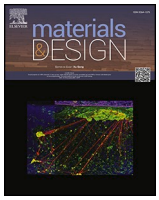
Materials & Design 260 (2025) 114993



Contents lists available at ScienceDirect

Materials & Design

journal homepage: www.elsevier.com/locate/matdes



Quasi-static crushing of DMLS-produced Ti6Al4V hierarchical honeycombs

M.I. Chibinyani [a,*], T.C. Dzogbewu [a], M. Maringa [b], A.M. Muiruri [a,b]

[a] Department of Mechanical and Mechatronics Engineering, Central University of Technology, Free State, Bloemfontein 9301, South Africa
[b] Department of Mechanical Engineering, Muranga University of Technology, Muranga 10200, Kenya

ARTICLE INFO

Keywords:
Lattice structures
Hierarchical honeycombs
Additive manufacturing
Surface roughness
Supports
In-plane loading
Energy absorption

ABSTRACT

Honeycombs excel at absorbing energy during quasi-static crushing events. Adding hierarchical structures to these designs improves their effectiveness. Hierarchical structures are best built using additive manufacturing technologies. There is, however, limited experimental data on their crush-resistance. This renders it difficult to improve and validate current theoretical and numerical models on the deformation behaviour of hierarchical honeycombs. This study aims to design vertex-based hierarchical honeycombs and examine their surface quality and mechanical behaviour for quasi-static crushing scenarios. Zero-, first-, and second-order hierarchical honeycombs were designed and fabricated using direct metal laser sintering technology. The Ti6Al4V specimens were quasi-statically crushed using the MTS Criterion™, Model 43 universal testing machine to evaluate the deformation behaviour of honeycomb topologies with different levels of hierarchy. Surface roughness analysis revealed that the average surface roughness (*Ra*) increased with the order of hierarchy, with lower *Ra* values on top flat surfaces compared to side inclined surfaces. Mechanical testing showed deformation occurred primarily through beam bending, with pronounced buckling under y-direction loading. The load drop after peak values was attributed to fracture at the vertices of the walls. The sequential collapse of the hierarchical honeycombs under compression began with the lowest order of hierarchy, involving bending, buckling, Poisson's ratio lateral expansion, and sliding along inclined and horizontal lines. Zero-order hierarchical honeycombs exhibited the lowest failure loads, while second-order hierarchical honeycombs had the highest. The design-to-experiment test approach was employed to predict the performance benefits of hierarchical honeycombs, providing valuable insights and highlighting design limitations to address crash-worthy additively manufactured hierarchical lattice structures.

1. Introduction

Design for fabricating structures with tailorable, complicated, and smart lattice geometries using the latest manufacturing technologies has significant impacts on their effectiveness as energy-absorbent [1–6] and impact-resistant materials [2,4,6,7]. Metal additive manufacturing technologies, particularly direct metal laser sintering (DMLS) or selective laser melting (SLM), part of the category of laser powder bed fusion (LPBF) [8–10], gives accurate control [8,10,11] and adaptability in design [9,10,12] when building hollow or lattice parts with complicated physical features. Such features are typically challenging to attain via traditional manufacturing methods, including casting, forging, machining and molding [13–15]. Using DMLS technology has numerous advantages [8–15] beyond its capacity for producing complicated shapes and customising parts minus the requirement for expensive tooling upgrades [14,15]. The aspect of adding materials in DMLS technology reduces generated waste particularly compared to subtractive manufacturing methods [15]. The metallic powder that remains after printing parts can be recycled and reused for fabricating structures in other projects as well [11,15]. The DMLS technology is also compatible with a range of metal alloys, including those of titanium, aluminium, and stainless steel [14,15]. The compatibility of DMLS with various metal alloys creates a broad selection list for engineering applications.

This paper is focused on the titanium-based alloy, Ti6Al4V, for use in the aerospace, automotive, defense and medical industries, particularly due to its high strength-to-weight ratio [17–20], corrosion resistance [16,17,21,22], durability at higher temperatures [16–18,21], enhancement of performance [16,17,20], reliability [16,17], fracture toughness [17,21], non-magnetic properties [23,24], ballistic resistance [25,26],

* Corresponding author.
E-mail addresses: chibinyanimunashe@gmail.com (M.I. Chibinyani), tdzogbewu@cut.ac.za (T.C. Dzogbewu), maringa@mut.ac.ke (M. Maringa), amuiruri@cut.ac.za (A.M. Muiruri).

https://doi.org/10.1016/j.matdes.2025.114993
Received 21 February 2025; Received in revised form 15 October 2025; Accepted 20 October 2025
Available online 22 October 2025
0264-1275/© 2025 The Author(s). Published by Elsevier Ltd. This is an open access article under the CC BY-NC-ND license (http://creativecommons.org/licenses/by-nc-nd/4.0/).

biocompatibility [16,18,19,21], and adaptability in design [17,27]. Though DMLS Ti6Al4V parts have numerous benefits, they additionally bring challenges and constraints that impact their functionality and effectiveness. The significant challenges are broadly classified as material-specific, process-specific, and application-specific challenges for additive manufacturing (AM) [28–30].

Over three decades, significant work has been reported on hollow or lattice geometries, including honeycombs (HCs) [6,31–44]. These hollow-built materials are designed to mimic the hexagonal unit cell configuration seen in organic HCs, with the primary objective of overcoming complex engineering problems [6,37,45]. The geometric configuration in HCs yields lightweight, yet strong and efficient designs, resulting in this type of lattice shape being advantageous for industries, such as aerospace, automotive, defense, medical, civil engineering, and packaging [6,38,45]. As materials science advances, applications and benefits of HCs are anticipated to broaden even further.

For the most part, quasi-static loads are used for analysing structures, including HCs [46]. A loading rate between 0.01 and 10 mm/min generally must be kept to in quasi-static crushing. Given the gradual application of load in this case, inertial effects are minimised, and the material's inherent mechanical characteristics predominate in the response of loaded structures [47]. For HCs, one of the primary features evaluated in quasi-static crushing is the capacity of the structure to absorb energy. Engineering fields that underline crashworthiness, packaging, and protective gear, extensive use is made of HCs in designing structures corresponding to their particular application [39–45]. The available literature in this field contains numerous reports of experimentation with various materials under quasi-static crushing, comprising aluminium, polycarbonate, and composites, in addition to leveraging polygon hollow shapes built using hexagonal, rectangular, triangular, and circular unit cells. These studies have repeatedly shown that, regardless of changes in the materials and configuration of the structure, the deformation modes and force versus displacement curve trends stay constant [6,38–44]. The bulk of work reported in open literature centres around analysing in-plane crushing behaviour particularly because polygon hollow parts are applied extensively for absorbing energies [39–44]. Mozafari et al. [48] investigated the impact of foam filling in aluminium HCs on their crushing behaviour under in-plane loads. Their findings showed that foam-filled HC can increase specific energy absorption by up to 20 folds and in-plane crushing strength by up to 208 folds. It was also observed that the effect of foam filling diminishes in denser HCs. As a result, increasing the mechanical properties pointed out in the preceding sentence is limited to 6 and 36 folds, respectively. Zhou et al. [49] thoroughly examined the in-plane quasi-static behaviour of a novel re-entrant combined-wall (RCW) HC, which was attained by integrating a hexagonal substructure in each inclined wall of the standard re-entrant (RE) HC. The analysis of the specific absorbed energy (SEA) revealed that the RCW HC outperforms the RE HC, with the SEA level approximately two-fold that of the latter. Choudhry et al. [50] used parametric modelling and geometric optimisation to examine the energy absorption capability of a customised re-entrant HC. It was found in their work that the newly developed HC outperformed a typical re-entrant HC by 36 % in terms of SEA. The crushing behaviour of HCs is known to be the result of an intricate combination of geometric design, and material characteristics. To optimise these structures for particular applications, it is imperative to carefully analyse and weigh these factors. Comprehending these impacting aspects allows the design of very effective and reliable HCs tailored to a wide range of engineering uses.

Hierarchical structuring in HCs is a powerful strategy reported in numerous studies [6,37,51–58], and its implementation has resulted in the fabrication of materials and structures with previously undocumented characteristics and functionalities. This design strategy for materials and structures is typically used to match the stringent requirements of contemporary applications by drawing inspiration from nature, in addition to leveraging advances in materials engineering [37,54]. This is in part because the hierarchical structuring of structures and materials enhances their mechanical properties and absorption of energies by integrating strength, toughness, fatigue resistance, and effective energy dissipation mechanisms [51,52,54–58]. These advantages are attained by mimicking the distinctive physical characteristics and interactions of biological structures at numerous scales, from the atomic to the macroscopic level [51,52]. In turn, new structures and materials with better mechanical characteristics in general can be produced. As noted in Fig. 1 of this document, there are four preferred strategies for generating hierarchical configurations, namely the vertex-based, cell-wall-based, fractal-based, and spiderweb-based, all of which are inspired by nature, where hierarchical structures are reportedly observed in a range of biological materials [51]. The analysis presented in this paper is centred around the vertex-based hierarchical HCs. Permission to reuse images shown in Fig. 1 has been obtained from ScienceDirect.

Recent reported advances in hierarchical lattice designs have impacted their use in defense, aerospace, automotive, medical, and energy industries [51,55–58]. As reported by Oftadeh et al. [55,56], the in-plane modulus of elasticity of hierarchical HCs improves substantially with increasing levels of hierarchy, resulting in enhanced effectiveness. Their findings showed that the first and second-order hierarchical HCs were 2.0 and 3.5 folds stiffer than traditional HCs and yet retained the same relative density. Zhang et al. [57] investigated SLM-printed $AlSi_{10}Mg$ hierarchical HCs under large deformation in the in-plane axes. Their findings indicated that higher levels of hierarchy substantially enhance the modulus of elasticity of HCs. Conversely, compressive strength improved negligibly. Their findings additionally showed a change of failure mechanism from cell wall bending to cell wall fracturing, when the density ratio and order of hierarchy increased. The findings also showed a direct correlation between failure mechanisms and the thickness of the wall with a critical value of 0.345 mm, indicating that below this threshold, the structure becomes significantly more prone to premature failure or instability. They concluded that the bending, axial compression, and shear deformation of the original unit cell walls are the primary causes of in-plane failure in hierarchical HCs. The same authors [58] later conducted plastic crushing failure analysis of corresponding geometries built via SLM using 316L stainless steel and $AlSi_{10}Mg$ materials. Under large deformation, the AlSi10Mg alloy HCs exhibited brittle responses, whereas the 316L steel HCs exhibited ductile responses, with a Poisson's ratio effect and gradient deformation of hierarchical unit cells. The application of unit cell advancements, such as optimised lattice designs, improved control of the inherent porosity of the structure, and refined wall thickness distribution, increased the modulus of elasticity of AlSi10Mg alloy HCs and advanced the densification mechanism of 316L stainless steel HCs by enhancing energy absorption and delaying localised failure. This study focuses on in-plane crushing to investigate the directional performance of hierarchical HCs. In-plane loading allows for a more detailed evaluation of deformation mechanisms, such as strut bending, buckling, and localised collapse, which are often challenging to observe in out-of-plane compression due to dominant layer-wise densification. Though in-plane crushing may not yield the highest energy absorption, it provides meaningful insights into in-plane stiffness, strength, and energy dissipation, key factors for applications involving lateral impacts or distributed loads. The limitations of this loading condition are acknowledged, and future work will include out-of-plane crushing to enable a full comparison of performance across loading directions.

Based on the studies reported in open literature that were available to the author [37,51–58], quasi-static crushing analysis for hierarchical HCs is limited to 316L stainless steel, $AlSi_{10}Mg$ alloy, and polylactides (PLA) materials. There is thus a clear need to conduct such tests using other metal alloys such as Ti6Al4V that are currently hot topics in DMLS or SLM research, and to examine their influence on the crushing behaviour of hierarchical HCs. The suggested quasi-static crushing testing of hierarchical HCs in this paper, that is additively built with

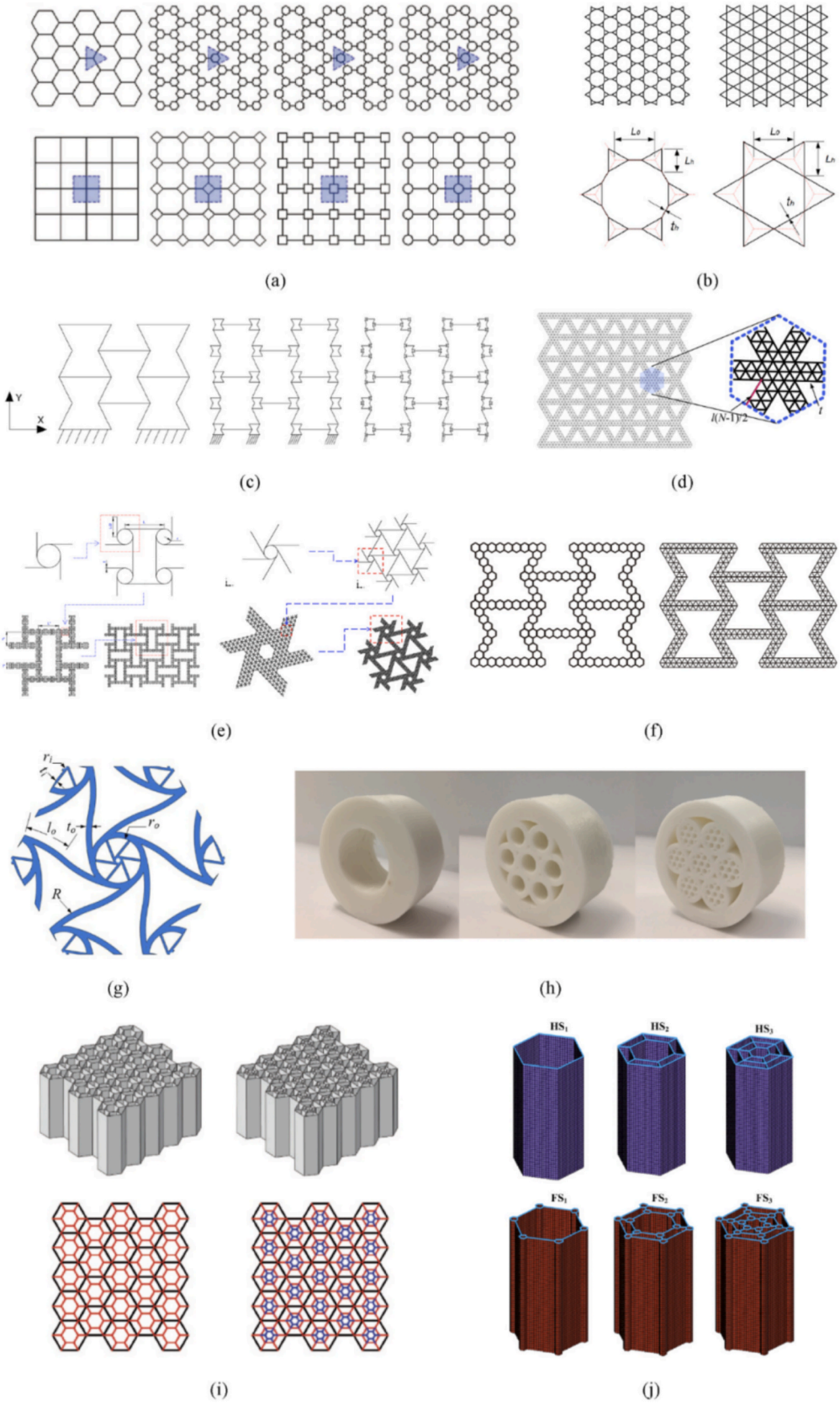


Fig. 1. (a-b) vertex-based hierarchical polygonal structures, (c) vertex-based hierarchical re-entrant HCs, (d) cell-wall-based hierarchical triangle honeycomb (HC), (e) cell-wall-based hierarchical using tetra-chiral and *hexa*-chiral HCs, (f) cell-wall-based hierarchical re-entrant HCs, (g) fractal-based hierarchical *hexa*-chiral HC, (h) fractal-based hierarchical circular polygon structures, and ((i-j) spiderweb-based hierarchical *hexa*-chiral HCs [51]. Example used with permission from Sciencedirect.com.

Ti6Al4V material is the first of its kind to the best knowledge of the author. The work could provide insights that advances understanding of the comparative benefits of Ti6Al4V in various related engineering applications. While various materials such as AlSi10Mg and 316L stainless steel have been widely used in the additive manufacturing of lattices and HCs, Ti6Al4V presents unique challenges and opportunities that remain underexplored, particularly in the context of hierarchical HCs. Compared to AlSi10Mg and 316L, Ti6Al4V is more difficult to process due to its high melting point, low thermal conductivity, and susceptibility to residual stresses and microstructural anisotropy during laser-based powder bed fusion. These factors complicate the fabrication of intricate hierarchical features, where dimensional accuracy and internal quality of struts are critical. Moreover, while AlSi10Mg and 316L offer good ductility, Ti6Al4V provides a significantly higher strength-to-weight ratio and superior fatigue resistance, attributes essential for load-bearing and energy-absorbing applications. However, these mechanical advantages are highly sensitive to the quality of build and post-processing, making Ti6Al4V both promising and technically demanding. By focusing on DMLS-processed Ti6Al4V hierarchical HCs, this study addresses the gap in understanding how this material's processing limitations and mechanical behaviour manifest in complex, multiscale architectures.

Additionally, there are limited details in reported studies describing all the particular energy absorption mechanisms determined during quasi-static crushing of hierarchical HCs. Comprehending the new findings reported in this paper, with reference to progression of deformation and failure mechanisms at various size scales inherently built in these structures, could provide critical value to various applications in engineering as well. By considering these findings before choosing a hierarchical design to adopt in an engineering application, grounds the insights of the designer while providing information on the anticipated effectiveness of the structure with reference to its corresponding reported deformation mechanisms. A ranking of the crushing behaviour for hierarchical HCs under two in-plane loading directions (the *x*- and *y*-axes), separately, has not been reported to date. The ranking now conducted in this work could facilitate a better understanding of the best directional behaviour suited for specific and advanced application of hierarchical HCs in engineering. Given that there are limited studies [37,52–58] on the deformation behaviour of hierarchical HCs as well, quasi-static crushing experiments must be repeatable and reproducible. The current experimental study on DMLS-produced hierarchical HCs adds to the bulk of reported material that can be used to ensure consistency of the crushing behaviours of such built structures.

To address these limitations, the research presented in this paper follows the systematic methodology shown in Fig. 2, with a primary objective to investigate the quasi-static crushing behaviour of DMLS-produced Ti6Al4V hierarchical HCs.

This paper is structured as follows. The hierarchical design, additive manufacturing, heat treatment, support structure removal, surface roughness assessment, and quasi-static experimental crushing methods for hierarchical HCs are described in Section 2, respectively. The most significant experimental findings are then highlighted in Section 3. These experimental findings are compared and discussed in the same section to provide an exhaustive summary of their impact on engineering applications. The way forward in designing hierarchical HCs is pointed out in the section that follows. The paper terminates in conclusions.

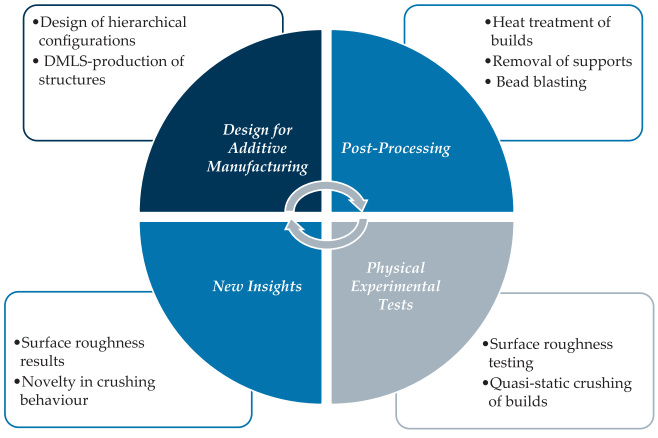


Fig. 2. A graphical outline of the systematic process used to attain new insights for quasi-static crushing of hierarchical HC builds.

2. Materials and methods

2.1. Design configurations of hierarchical parts

First and second-order vertex-based hierarchical HCs were built based of a regular HC. The adopted HC structure features basic geometric parameters, such as the sloping angle $\theta = 30^{\circ}$, cell wall length l, and thickness t, shown in Fig. 3 [59]. The permission to reuse the illustrations shown in Fig. 2 has been obtained from ScienceDirect.

In a case where the same design parameters are assigned to the 1st- and 2nd-order vertex-based hierarchical HC configurations, the parameter t must decrease in value. Fig. 4 shows the relationship between the parent HC structure and its corresponding self-similar hierarchical configurations using geometrical features [60]. Permission to reuse the example shown in Fig. 3 has been obtained from ScienceDirect.

The ratio of the set hexagonal edge lengths describes the structural configurations of the HC at each level of the hierarchy. In this scenario, the hexagonal edge length for the 1st-order hierarchical structure is represented by symbol b, and c corresponds to the 2nd-order hierarchical structure, with the original hexagon's edge length being represented by symbol a, shown in Fig. 4 [60]. The ratios of the edge lengths for the 1st- and 2nd-order hierarchical HC structures with respect to that of the regular or zero order hierarchical structure can be written as $\gamma_1 = b/a$ and $\gamma_2 = c/a$, respectively. The 1st-order hierarchical HC structure is governed by the interval $0 \leq b \leq a/2$, and where the regular structure is described $\gamma_1 = 0$, this interval becomes $0 \leq \gamma_1 \leq 0.5$. For the case of the 2nd-order hierarchical HC structure, either one of the two intervals, namely $0 \leq c \leq b$ or $c \leq a/2\text{-}b$ could be adopted as the geometrical constraint. The ratio parameters can be presented in intervals as well. Given the case where $\gamma_1 \leq 0.25$, this results in an interval of $0 \leq \gamma_1 \leq \gamma_2$, and where it falls in the range $0.25 \leq \gamma_1 \leq 0.5$, the interval becomes $0 \leq \gamma_2 \leq (0.5\text{-}\ \gamma_1)$ [35]. The dimensionless specific relative density, or the area fraction, could be expressed with regard to the ratio t/a, as shown in Equation (1) [60].

$$\rho = 2\sqrt{3} \bullet (1 + 2\gamma_1 + 6\gamma_2) \bullet t/a \tag{1}$$

In the design of hierarchical HC parts, the particular cases of γ_2 and

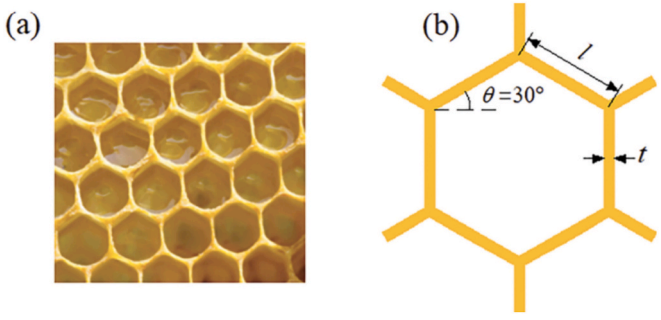


Fig. 3. (a) The HC beehive seen in nature and (b) the regular unit hexagonal cell shape used to design HC [59]. Example used with permission from Sciencedirect.com.

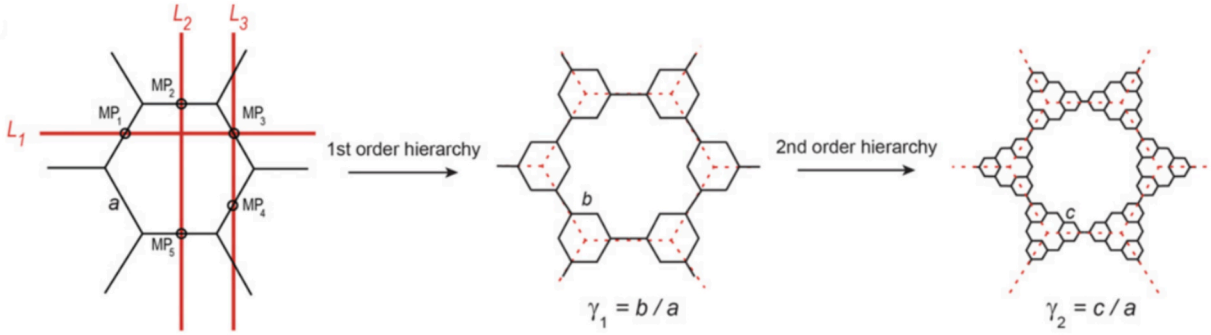


Fig. 4. The relation derived between the basic HC structure and its corresponding self-similar hierarchical configurations [60]. Example used with permission from Sciencedirect.com.

$\gamma_1 = 0$ can be ignored given that t corresponds to the original wall thickness. For regular and 1st-order hierarchical HC parts, the relative densities are written as seen in Eqs. (2) and (3), respectively [60].

$$\rho_0 = 2\sqrt{3} \bullet 2t/a \tag{2}$$

$$\rho_1 = 2\sqrt{3} \bullet (1 + 2\gamma_1) \bullet t/a \tag{3}$$

Ajdari et al. [60] highlighted that the relationship deduced from the analytical models they developed for hierarchical HC structures suggests that as γ_1 and γ_2 increase, t/a decreases so as to maintain a fixed relative density. Fig. 5 shows computer-aided designs (CAD), including the regular and its corresponding self-similar hierarchical HC configurations with $\rho = 0.10$ and $a = 20\ mm$, which were generated using SolidWorks design software (version 2021 SP5). The regular HC was assigned a value of $t = 1.75\ mm$; the 1st-order hierarchical HC structure was assigned values of $\gamma_1 = 0.3$ and $t = 1\ mm$; in addition, the 2nd-order hierarchical structure was assigned values of $\gamma_1 = 0.3$, $\gamma_2 = 0.12$, and $t = 0.75\ mm$. These assigned values are often used and considered reliable in design and manufacturing of structurally stable hierarchical structures [60].

In HC designs with hierarchical configurations, the uniform wall thickness of higher orders is reduced progressively to maintain the same relative density. Hierarchical HC parts produced via additive manufacturing, as detailed in the following subsection, may struggle to consistently achieve the ideal apparent densities due to factors such as process variability, material inconsistencies, geometry and build orientation, thermal stresses and warping, porosity formation, and post-processing effects. In addition, the particular discrete values of γ_1 and γ_2 can prove difficult to obtain as well because of failure to attain the ideal apparent densities. Therefore, a relative density range of *7.5–12.5 %*, was selected in the present work to account for such inconsistencies. This range is typically selected to ensure that the structure performs close to its intended design parameters even with these potential inconsistencies.

2.2. Additively-produced hierarchical honeycomb parts

An entire set of twelve Ti64Al4V (ELI-extra low interstitial) hierarchical HC parts were printed at the Centre for Rapid Prototyping and Manufacturing of the Central University of Technology, Free State, South Africa. These parts were built using a direct metal laser sintering (DMLS) EOSINT *M290 400 W* machine based on the CAD files used to develop the hierarchical structures shown in Fig. 5. A titanium base plate was used as a substrate, and argon gas circulated within the build chamber during printing. A minimum wall thickness of *0.75 mm* for all the builds was maintained to prevent challenges associated with printability and process control, surface quality and resolution, heat dissipation, and post-processing requirements. After printing, the parts were cooled to temperatures below *60 °C* before being removed from the machine. This was done to prevent the builds from warping. Fig. 6(a) shows four printed regular HC builds before they are cut off from the build plate. Three different hierarchical HC builds right after they are cut off from the build platform are also shown in Fig. 6(b).

For reproducibility of the hierarchical HC parts, Table 1 shows the EOSINT M 290 DMLS processing parameters that were adopted in this study. Additionally, Fig. 7 shows the scan strategy that was used for printing the parts [61].

The structures depicted in Fig. 6 require both stress relief and high-temperature heat treatment. The temperatures and soaking periods used for both stress relief and high temperature heat treatment are described in the subsequent section. Stress relieving addresses the residual stresses that emerge in SLM as a result of the layer-like process and the restrain of current layers by previous layers from contracting. This is done before removal of built parts from the support base to prevent warping. High temperature heat treatment, on the other hand, addresses the existence of martensitic needle-like structures formed due to the rapid cooling rates of built parts that are greater than 460 °C/s and the attendance brittleness of printed parts [62].

2.3. Heat treatment protocol used on As-Built Ti6Al4V hierarchical honeycomb parts

The twelve parts manufactured using DMLS technology, including the as-built regular HC and the 1st- and 2nd-order hierarchical HC, were first stress relieved before being separated from the substrate. This stress relieving regime is what is recommended by the manufacturers for the Ti6Al4V(ELI) built in the DMLS EOSINT M290 machine. The parts were then heat treated using a high temperature two-stage annealing protocol. The two-stage annealing process on the as-built Ti6Al4V parts was carried out to improve their ductility at the cost of reduced strength. This heat treatment protocol is typically used when Ti6Al4V builds with a bimodal microstructure is required [63]. Fig. 8 shows the graph that is generated by the input file of the furnace program for two-stage high-temperature annealing.

The Ti6Al4V(ELI) regular HC and HC hierarchical parts were first stress-relieved in a pre-heated furnace at *650 °C* for *180 min*. This was followed by their heat treatment through two stages of high-temperature annealing. The final temperature in this heat treatment was set to *990 °C*. The specimens were soaked at this temperature for *90 min*. The chosen temperature is slightly higher than Ti6Al4V's beta transus temperature of *980 °C*. This is to allow complete decomposition of the martensitic alpha microstructure and stimulate the globularisation of the resulting beta grains. The Ti6Al4V(ELI) parts were then furnace-cooled to *760 °C* and soaked at this temperature for *120 min*. This was done to allow coarsening of the formed alpha grains. In the last stage of this heat treatment, the Ti6Al4V(ELI) parts were slowly cooled to room temperature in the furnace by increasing the flow of argon gas in it.

Though microstructural analysis using scanning electron microscopy (SEM) or electron backscatter diffraction (EBSD) of the treated

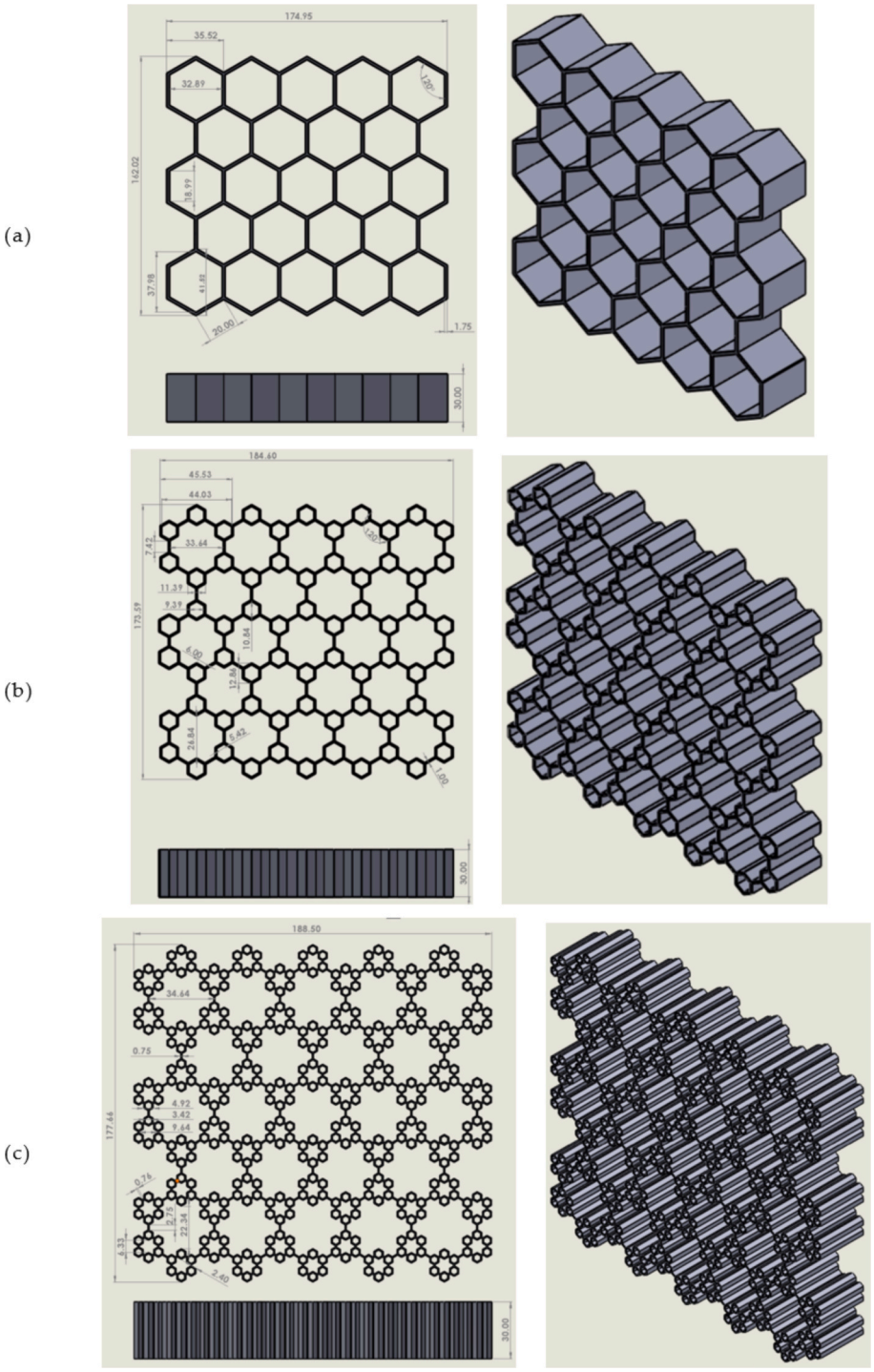


Fig. 5. Hierarchical CAD designs and dimensions, (a) regular HC, (b) 1st-order hierarchical HC, and (c) 2nd-order hierarchical HC.

specimens was not performed in this study, the effectiveness and the anticipated outcomes of this heat treatment strategy are thoroughly substantiated in literature. Comparable microstructural evolutions, particularly the dissolution of martensitic structures and the formation of stable $\alpha + \beta$ phases, have been documented in separate studies by Muiruri et al. [64], and Malefane et al. [65], both conducted within the same research group and laboratory as the present work. Their research corroborates the correlation between such thermal profiles and the resultant enhancements in mechanical properties, thereby validating the heat treatment approach employed in this investigation.

2.4. Removal of supports from the hierarchical honeycomb parts

The supports were printed vertically, along the z-build direction of the Ti6Al4V(ELI) regular and hierarchical HC builds. It must be noted that the DMLS-printed structures in this work are complex in geometry, with an enhanced ductility as a result of the high temperature two-stage annealing that was performed. The hydraulic press, tools and parts shown in Fig. 9 were used to remove the supports from the printed hierarchical HC parts.

The supports were pressed out as shown in Fig. 9, using different shapes and sizes of metal bars and rods. Loads in the range 4–12 MPa,

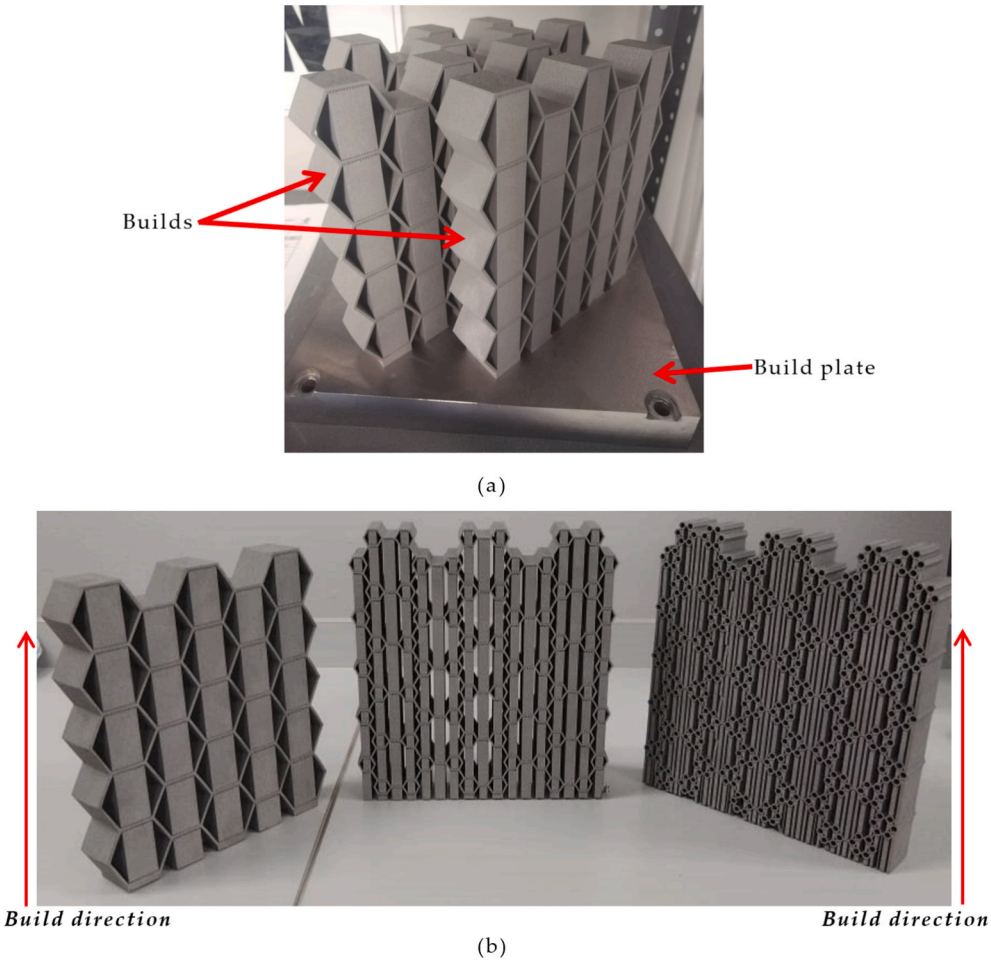


Fig. 6. Additively-produced parts, (a) regular HC parts before being cut off from the build plate, and (b) from the left to the right are images of the regular HC, 1st-order hierarchical HC, and 2nd-order hierarchical HC after being cut off from the build plate, respectively.

Table 1
EOSINT M 290 DMLS processing parameters [61].

Processing Variable	Value
Laser power setting	175 W
Laser diameter	80 μm
Hatch spacing	100 μm
Layer thickness	30 μm
Scanning speed	1400 mm/s

were used to press out the supports for the smallest to the largest cross-sectional areas of supports, respectively. It is recognised that such loads could result into deformation of the structures and better methods should be developed to carry out this exercise. The spread of these loads on the structure was minimised through the use of a thick stainless-steel plate with holes that ensured localization of the applied loads on the supports rather than the hierarchical HCs. The minor support pieces that still remained on the Ti6Al4V(ELI) builds even after using of the hydraulic press were cleared off using a rubber mallet and chisel, which is a further cause for concern on the structural integrity of the final parts. The result of this exercise for the three different Ti6Al4V(ELI) hierarchical HCs is the three images shown in Fig. 10.

The process of removal of supports in this investigation was found to be time-consuming, laborious, and resource-intensive. More critically, the volume of scrap metal generated during the removal of support structures surpassed that of the final components. Specifically, a total of 11.34 kg of Ti6Al4V(ELI) scrap was produced, compared to 5.93 kg for all twelve hierarchical honeycomb (HC) structures, resulting in a waste-to-use ratio of 1.91:1. This result contradicts the widely advocated advantage of additive manufacturing (AM) as a low-waste fabrication method.

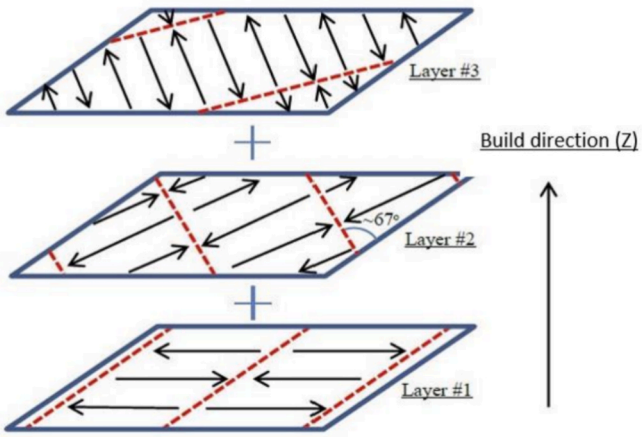


Fig. 7. Schematic illustration of the strip-scan pattern employed in the EOSINT M 290 system, depicting raster scan vectors (indicated by arrows) within individual stripes (bounded by dashed lines). With each successive layer, the scan stripes are rotated by 67° relative to the orientation of the previous layer to promote uniform material properties and reduce anisotropy [61].

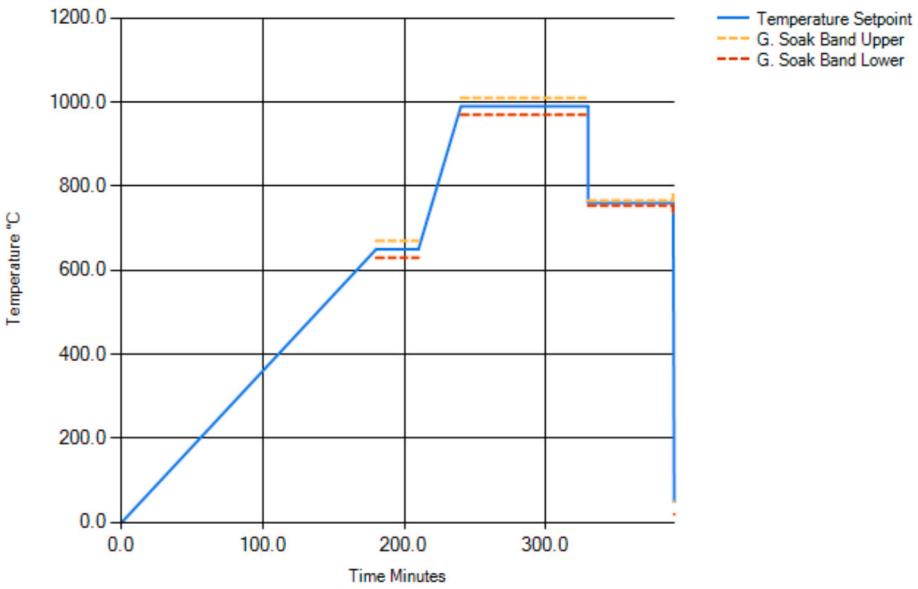


Fig. 8. A two-stage high temperature annealing curve for Ti6Al4V(ELI) hollow parts.

The substantial volume of support waste emphasizes the pressing need for optimisation of support strategies, especially in the fabrication of geometrically complex structures such as hierarchical lattices. Future research should incorporate techniques for reduction of supports at both the design and build preparation stages, which includes optimised part orientation, the utilisation of self-supporting geometries, lattice-based supports, and algorithmically generated low-volume support designs. Moreover, the integration of alternative support materials, such as water-soluble or acid-soluble alloys in hybrid builds, presents potential for significantly reducing post-processing waste and enhancing efficiency of material-usage [7,13,15,27]. The accumulated metal scrap resulting from support removal is depicted in Fig. 11.

2.5. Surface roughness testing for hierarchical honeycomb parts

Surface roughness was measured on four Ti6Al4V(ELI) parts that were selected randomly. This consisted of one regular HC, two 1st- and 2nd-order hierarchical HCs, and a fourth 1st-order hierarchical HC build that was blast smoothened on three faces of the flat side surfaces for a period of two hours. The three flat surfaces of the smoothened faces were used to determine if the bead blasting strategy had a significant effect in smoothening the surfaces of the Ti6Al4V(ELI) built parts. An automated shot peening strategy, using round stainless-steel beads on the flat surfaces of the build was adopted. This protocol was conducted following the SAE standard, AMS 2430: 2014.

Surface roughness for each selected face was measured at 12 different points and the average and standard deviation calculated. The surface roughness was measured using a Mitutoyo surface roughness tester (SJ-210). This instrument was first connected to a computer running the Surftest SJ-210V.1.008 software package. The specimen was first calibrated using the ISO 4287: 1997 standard, as described in the manual for the equipment. During testing, the cutoff length (the length over which the roughness is evaluated) of 2.5 mm was assigned to determine the R_a value. The surface roughness of three top flat faces and three side inclined faces for each of the selected Ti6Al4V(ELI) builds was measured. The R_a measurement indicates the profile's mean arithmetic deviation of the peaks and crests from the mean line, R_z the average of consecutive highest peaks or crest or average distance between the highest peak and lowest crest, and R_q the distance of the highest peak from the mean line (R_p) or the distance of lowest crest from the mean line (R_v). Surfaces with low values of these three roughness indicators are typically regarded as smooth. Roughness in the present work was determined using the R_a value, which corresponds to a component's overall surface roughness. The surface roughness of the bead blasted Ti6Al4V(ELI) structure was only evaluated for the top flat faces. Inclined surfaces cannot be effectively smoothed because geometries built at any angle other than 90 or 180 degrees are not well exposed to direct blasting of the beads, diminishing overall smoothing effectiveness.

2.6. Quasi-static crushing analysis of hierarchical honeycomb builds

An MTS Criterion™, Model 43 universal testing machine was used to perform quasi-static crushing tests on twelve Ti6Al4V(ELI) hierarchical HC parts manufactured via DMLS. Fig. 12 shows the setup used to carry out these test.

Two builds of each of the four manufactured Ti6Al4V(ELI) regular HC parts were loaded along the *x*-axis, with loads applied directly on their flat surfaces, as illustrated in Fig. 12(a). The remaining two sets of regular HC parts were loaded along the *y*-direction, which meant that the loads were imposed directly on the apexes, as shown in Fig. 12(b). A testing safety cage made of mild steel sheets with a thickness of 2 mm and length, width, and height dimensions of 380 × 286 × 200 was used to shield operators from objects flying of the structures during crush tests. A digital *Nikon* camera was also positioned such that it captured the deformation process of the Ti6Al4V(ELI) parts during the crush tests. Before starting quasi-static compression, the MTS Criterion™, Model 43 universal tester was set to zero load and then a load rate of *5 mm*/min set. To facilitate comparison of the crash tested specimens, the greatest displacement of the Ti6Al4V(ELI) HC parts under the specified crush load rate was fixed at *160 mm*, in addition to the machine's limiting load, which was set at *29.5 KN*. The foregoing procedure was used to crush first- and second-order hierarchical HC builds, as well.

3. Results and discussion

3.1. Surface roughness

Surface roughness tests were performed to evaluate the quality of HC parts at various hierarchical levels. Figs. 13, 14 and 15 feature the results of surface roughness measurements for zero-order, 1st-order, and 2nd-order hierarchical HCs measured directly on the top flat and side inclined faces, as well as data measured directly on the top flat faces of a bead-blasted 1st-order hierarchical HC. The figures include average values and standard deviations.

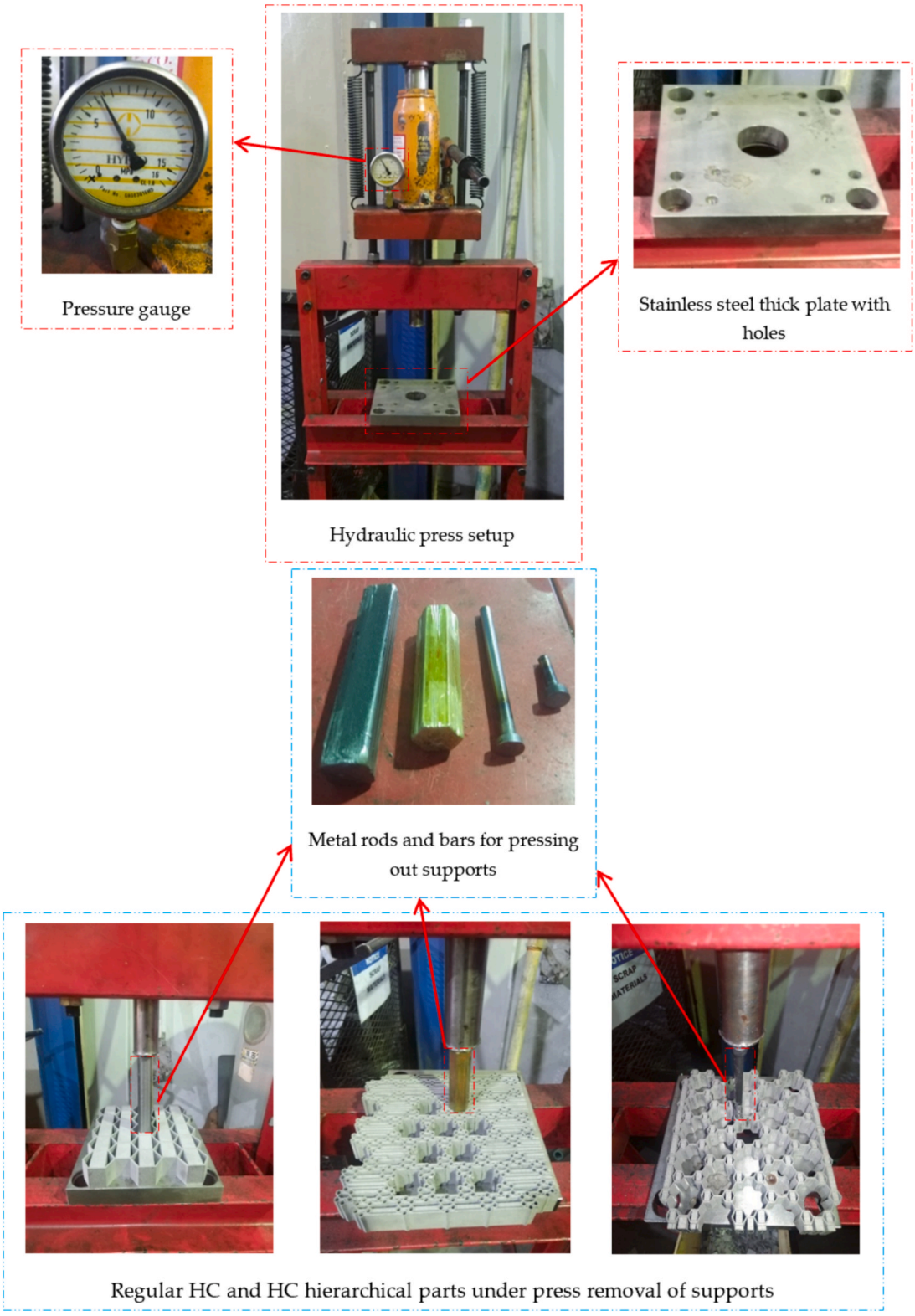


Fig. 9. The setup used for pressing out supports in hierarchical HC parts.

The coefficient of variance (CoV) is calculated for each set of data; mean and standard deviation reported in the two figures that preceded to identify if the values of mean have a statistical meaning. This calculated CoV is based off the data set measured for the top flat and side inclined faces of each level of hierarchical HC builds, separately. The zero-order, 1st-order, and 2nd-order hierarchical HCs have percentage values of 1.250 %, 9.562 %, and 8.485 %, respectively, for the CoV calculated based on the mean and standard deviation of *Ra* at the top flat faces. The inclined surfaces of the same hierarchical HCs stated in the previous sentence have percentage values for CoV of 4.106 %, 12.562 %, and 2.156 %, respectively. Typically values of CoV less than 5 % denote clustering and imply that the values of mean have a statistical meaning. Large values of CoV imply large scatter of data away from the mean, which implies the mean has no statistical value [62]. From the

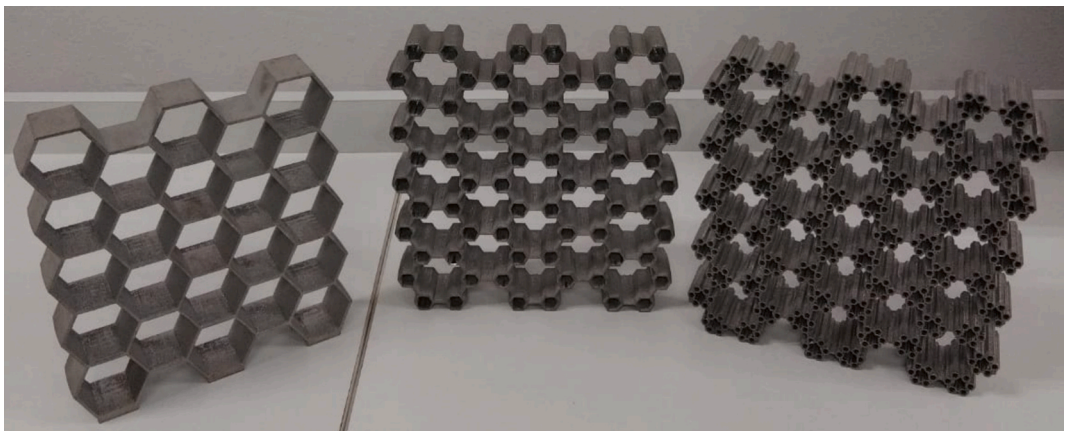


Fig. 10. The regular HC and its hierarchical parts produced via DMLS technology.



Fig. 11. Ti6Al4V(ELI) scrap resulting from removing supports of DMLS-produced hierarchical HC parts.

perspective of the mechanical properties of metallics in general, constructed Ti6Al4V(ELI) hierarchical HCs with percentage changes in CoVs limited to no more than 5 % indicates surface roughness measurements that are more accurate and closer to the true value [66,67].

It is also garnered from Fig. 13 that the there is a gradual increase of the mean surface roughness with increasing order of hierarchy and a sharp drop arising from bead blasting. Smoothing out the top flat faces of the 1st-order hierarchical HC structure resulted in a 1.479 μm drop in *Ra* value, which a significant 18 % of the value for the unblasted surface. This implies the effect of bead blasting on surface roughness is significant considering the only two-hour bead blasting period used in this case. Thus where surface roughness is critical, the process may be applied to reduce its magnitude. For the side inclined faces, Fig. 14 reveals a similar trend as the one observed in the previous figure, with *Ra* values increased with increasing order of hierarchy for the three hierarchical HCs. The result of this analysis shows that the side inclined sides of the 2nd-order hierarchical HC structure have the highest value of the mean surface roughness. The authors identify a knowledge gap on how different hierarchical levels affect surface quality. This forms part of their ongoing investigations on how geometric complexities, such as larger surface areas and variations in texture introduced by higher hierarchy levels, contribute to higher *Ra* values.

Fig. 15 depicts the grouped surface roughness findings from the preceding two figures. The bar graphs in this figure clearly show the magnitude of the mean surface roughness to be greater for surfaces on the side inclined faces than on the top flat faces. For the zero-order, 1st-order, and 2nd-order hierarchical structures, the magnitudes of *Ra* for the side inclined faces were 62.71 %, 57.79 %, and 58.55 %, times higher than the values for the top flat surfaces, respectively. Therefore, in cases where surface roughness is critical, such as use of hierarchical structures for transportation of fluids, this big difference demands use of methods for smoothening surfaces in order to have similar values for all surfaces.

An increase in hierarchical level is consistently associated with higher surface roughness (*Ra*). This correlation is primarily driven by the increased geometric complexity inherent to higher-order structures, which imposes significant challenges during the DMLS process. Specifically, the presence of intricate overhangs, fine features, and enclosed regions restricts effective heat dissipation and impedes evacuation of powder, thereby promoting partial melting and the adhesion of particles of powder to one another. These geometric-induced effects lead to irregularities such as balling and formation of spatter particles, which lead to further deterioration of the quality of surfaces [68]. The severity of these phenomena is governed by key DMLS process parameters, most notably laser power and scanning speed, which control thermal gradients, and solidification rates during fabrication. Substandard selection of process parameters can destabilise the melt pool, exacerbate the formation of surface defects and increase roughness. This is supported by the work of Yadroitsev et al. [69], who demonstrated that while higher laser energy densities increase surface hardness in DMLS-fabricated Ti6Al4V(ELI), they also lead to more pronounced surface defects when not adequately tuned, due to phenomena such as keyholing and excessive remelting. Therefore, the observed increase in surface roughness with increasing hierarchy level must be understood as a coupled effect of geometric constraints and process parameter interactions. To improve surface morphology in complex hierarchical structures, localised optimisation of DMLS parameters should be considered, adapting laser exposure strategies to specific geometric features.

The surface roughness increases with hierarchy level, primarily due to smaller strut diameters or thickness and more complex laser scanning paths. While its direct impact on mechanical performance has not been quantified, surface roughness is known to significantly influence the initiation of fracture and stress concentration, particularly in Ti6Al4V, which has limited ductility and is highly sensitive to surface defects [27,69]. Increased roughness can promote early initiation of cracks, reduce fatigue life, and alter local distribution of stress. These effects are likely to be more pronounced in higher-order hierarchical structures, where thinner features are more susceptible to localised failure [69]. Though global buckling and collapse of cells were seen to dominate the

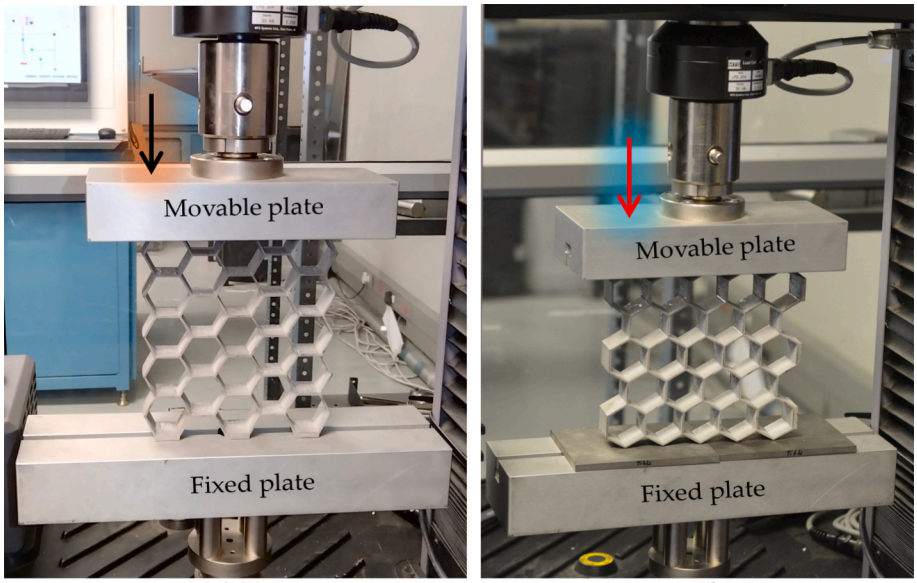


Fig. 12. Compression experimental setup using MTS CriterionTM, Model 43 universal tester for: (a) a regular HC loaded in the x-direction, and (b) a regular HC loaded in the y-direction

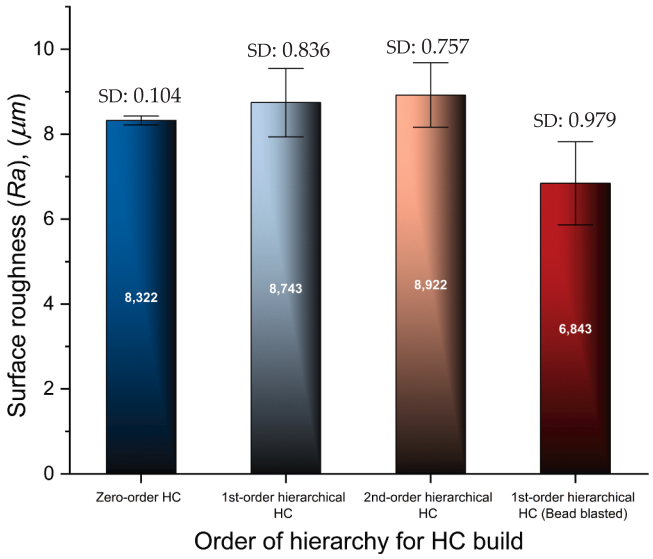


Fig. 13. The mean surface roughness (Ra) of the surfaces of the top flat faces of the various levels of hierarchy for HCs.

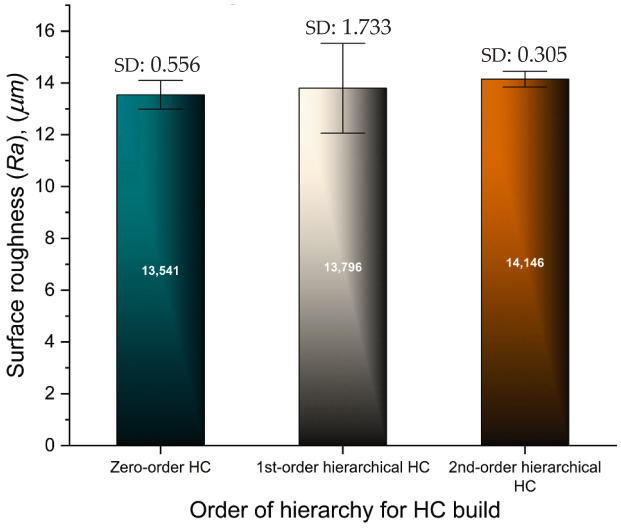


Fig. 14. The mean surface roughness (Ra) of the surfaces of the side inclined faces of the various levels of hierarchy for HCs.

deformation behaviour in this study, future work should examine how surface roughness contributes to failure mechanisms, using high-resolution imaging, digital image correlation, or numerical modelling that accounts for surface irregularities.

3.2. Mechanical behaviour

The effect of x-direction crushing. The evolution of deformation and fracture for each tier of hierarchical HC loaded in the *x*- and *y*-directions separately were examined by a video recording throughout the crushing tests. Camera images for each notable peculiar change in shape and fracture patterns for all the tested structures, for loads applied along the *x*- and *y*-directions, are presented in Figs. 16 and 17, respectively.

The evolution of deformation shown in Fig. 17 (for *x*-directional loading) reveals that bending loads on the primary walls (walls building the larger unit cells) are predominant and cause out-of-plane deflections of these walls to occur. As the compression load increases, the bending mechanism of the primary walls transitions into fractures in regions closer to the vertices of the primary walls. The regions closer to the vertices where fracture first occurs is highlighted by red circles with a dotted lines for each level of hierarchical shown in this figure.

For all the structures presented in this figure, the identified areas of first fracture identified by the red dotted circles are aligned along an inclined line. During failure, the cell walls were observed to deform through bending and fail by sliding down this inclined line to the point where entire layers of primary unit cells comes into contact with one another, as highlighted by the red shading in the third right images in Fig. 16. During sliding of primary cell walls along the inclined line, the load continues to drop up until the primary cell walls come fully in contact. At this point, a set of primary cell walls for the next higher order of hierarchy starts to deform and then fracture at the vertices in a similar manner, thus leading to a similar deformation and sliding as occurred for the lower order of hierarchy. Where there is an even higher order of

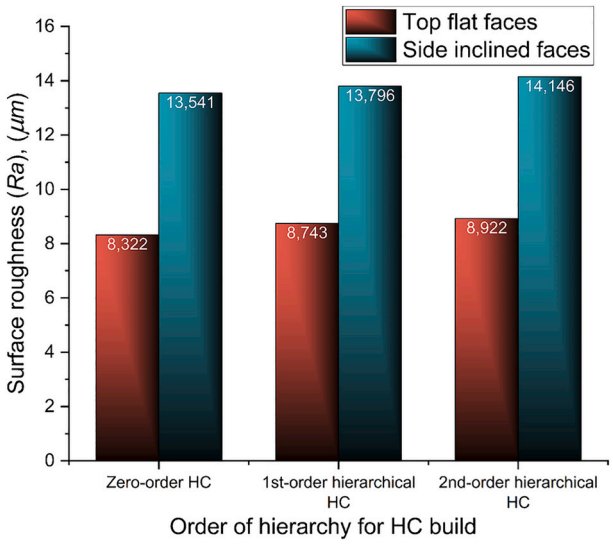


Fig. 15. Grouped values of mean surface roughness for the top flat and side inclined faces.

hierarchy, the process repeats itself. This continues till all of the primary cell walls are stacked and in full contact with neighboring ones, as illustrated in the far-right images of the different orders of hierarchy shown separately in Fig. 16.

The effect of y-direction crushing. Though bending loads retain their predominance in the deformation of primary walls under the influence of *y*-directional loading, there are indications of buckling occurring in the vertically configured primary walls of the different levels of hierarchical structures whose camera images are presented in Fig. 16. In contrast to the case for *x*-directional loading, the earliest stages of fracture occur at vertices of the primary walls along horizontal lines, that have been identified in Fig. 17, by dotted red circles.

Gibson and Ashby's foundational research [70], along with later studies [6,31–44,51,71], noted that the slender cell walls of HCs are prone to buckling under compressive in-plane loads. When a y-directional load is applied, vertical sections of the cell walls compress, further increasing the risk of buckling.

For loading in the *y*-direction, the primary cell walls after the first stages of fracture resort to sliding horizontally. This continues until adjacent primary cell walls are in full contact as shown by the red shading of the various levels of hierarchical structures shown in Fig. 17. One full contact is attained, the process repeats itself for the next order of hierarchy and so on until all of the primary walls are stacked and in contact with neighboring ones, as confirmed by the far-right images for each order of hierarchy shown in Fig. 17.

Deformation of hierarchical HCs was found to be predominantly due to bending loads. This is similar to what has been reported in numerous studies [40–44,48,51,55–58,63,66]. The observation is acceptable given the fact that the structures were built of thin walls and beams, which typically have low bending stiffnesses. As the applied loads increased, the structures experienced fracture at the vertices of primary walls. This is consistent with observations made in [58]. The vertices where the walls converge are known to be sites of stress concentration and are therefore, expected to experience higher stress levels than the other areas of the structure given that the load paths converge at these points. The deformation, fracture and sliding behaviour observed in this work has only been noted for zero-order HC structures [6,31–44] and is therefore novel in its extension to higher orders. Moreover, the different inclination of sliding for loading along the *x*- and *y*-directions, separately, is peculiar to the present investigations.

Influence of the particular order of hierarchical structure. Further observations regarding the crush loading and the attendant deformation trends of the zero-order HC configuration, independent of the direction of loading (*x* or *y*) are made based on the camera images shown in Fig. 18. The images reveal that, besides bending deflections and buckling deformation of the primary cell walls, some unit cells under crushing loads exhibit as the Poisson's ratio effect for loading along both the *x*- or *y*-directions. Beyond this, the zero-order HC exhibited deformation and sliding until all of the cell walls established full contact with neighboring ones, at which point densification of the material started.

Since the lengths of the primary cell walls reduce as the hierarchy level in HCs increases, the magnitude of bending and buckling decrease as well. Moreover, as has been noted in the preceding discussion in this section, each order of hierarchy experiences similar crushing behaviour in a consecutive trend from the lowest to the highest order of hierarchy. Examples of this are shown Figs. 19 and 20 for the 1st and 2nd orders of hierarchy, respectively. This implies that the stiffness of the different hierarchies increases with increasing orders of hierarchy. These two considerations imply that the amount or energy absorbed during crushing will increase with increasing order hierarchy. Furthermore, this implies that the Poisson's ratio effect observed in zero-order HCs reduces with the increasing stiffness of higher hierarchical levels. This experimental finding is consistent with literature that reports on Poisson's ratio effect on hierarchical HCs from theoretical models [55–58,63,66]. In zero-order HCs, the load is distributed via a more basic network of cell walls. This implies that the transverse strain response to an axial load for this order is less complicated and simpler to observe. Distribution of load in higher levels of hierarchical HCs gets more complicated as the number of layers and interconnecting networks of cells increases, which could obscure or diminish the Poisson's ratio effect in experimental testing.

The observed further crushing events for each higher order of hierarchy implies that higher orders hierarchy in HCs are more crashworthy. These crushing events are a function of hierarchy and the attendant scaling effects. For HC's hierarchical designs, smaller-scale structures were seen in the present work to support larger-scale ones in a progressive process of failure from large scale to small scale structures.

It also stands to reason from the foregoing discussion that even as irreversible failure is experienced at lower levels of hierarchy, elastic recovery of higher levels of hierarchy will still occur after removal of the applied load.

Effects of loading direction on energy absorption in various hierarchical levels. The results in Fig. 21 are used to rank mechanical properties of all twelve DMLS-produced Ti6Al4V(ELI) specimens in terms of loading direction and hierarchical order. Since there were four specimens for each hierarchical level examined, numerals 1 and 2 were placed right after the prescribed *x*- and *y*-loading directions, which are indicated in brackets in the legend to differentiate their findings. Numerals 1 and 2 represent the first and second specimens in the prescribed direction of loading.

The load curves for loading HCs with various hierarchical levels in the x- and y-direction independently (Fig. 21) show a general trend showing the increase in load and subsequent drop due to failure and further increase followed by drops, and so on. The load curve behaviour follows a sequence of deformation, fracture, and sliding discussed previously in this section, that now explains the rise and drop pattern. Initially, the primary cell walls experience bending due to the load, causing out-of-plane deflections. As the load increases, bending transitions into localised fractures near the vertices of the primary walls. After fracturing, the walls begin to slide along an inclined path, resulting in a sudden drop in the load as the primary unit cells move closer together. Once these walls come into full contact, the load starts increasing again as the next level of hierarchy begins to deform, repeating the process. This cycle of bending, fracturing, and sliding continues through each hierarchical level until all walls are stacked in contact, explaining the repeated increases and drops in the load curve.

There is a clear difference between the height of the load drops for zero-order HCs loaded in the x- and y-directions, shown in Fig. 21(a),

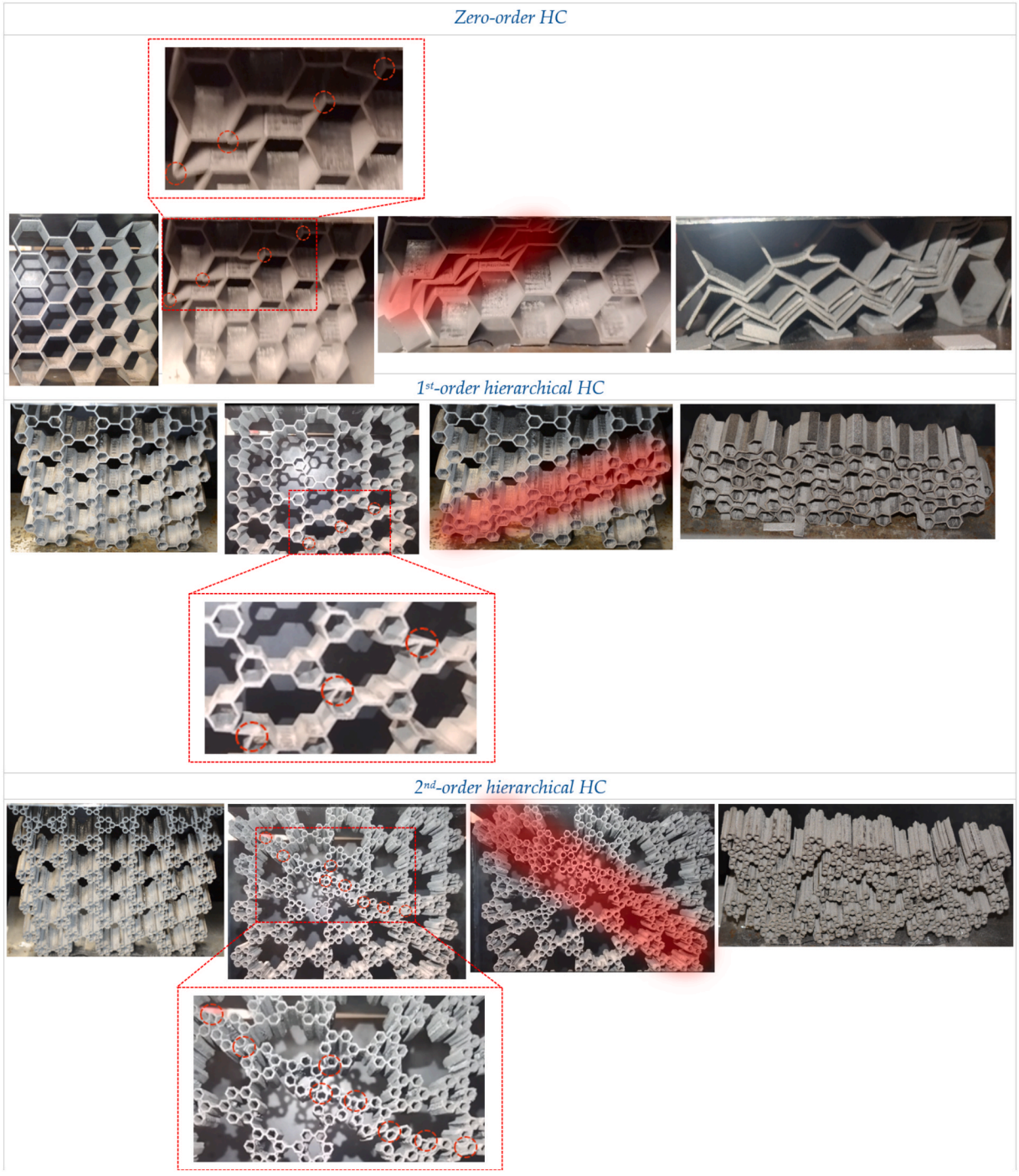


Fig. 16. Evolution of deformation, fracture and bulk sliding in the three levels of hierarchical HCs under x-directional loading.

where the former drops much lower. This difference in height is seen to diminish for higher hierarchical levels shown in Fig. 21(b, c). This implies that at lower hierarchical levels, deformation and failure mechanisms are more directionally dependent, with lower resistance in certain orientations. As the hierarchical level increases, the structures behaviour tends to be more similar in the orthogonal directions, in terms of distributing loads more evenly across different directions, leading to more uniform deformation and failure behaviour. This indicates that higher levels of hierarchical structures enhance structural stability [67] and reduce directional sensitivity.

There is also a clear reduction of the height of the load curves following the first peak and then consistent increase in the peaks for ensuing cycles to a point where the final peaks are higher than the initial one observed for HCs of higher hierarchical levels, as shown in Fig. 21(d, e). This implies that the deformation and failure mechanisms in HCs of higher hierarchical levels evolve with each cycle. The initial reduction indicates that early deformation and fracture primarily weaken the structure at the beginning, especially as localised fractures occur near the vertices of the primary cell walls [58]. The increasing peaks in later cycles imply that after initial failure, the structure stabilizes as layers of primary cell walls come into full contact. This stacking effect likely strengthens the HC, allowing it to bear higher loads as the hierarchy continues to deform and fail in a more controlled and uniform manner, ultimately leading to stronger resistance in later stages. This pattern

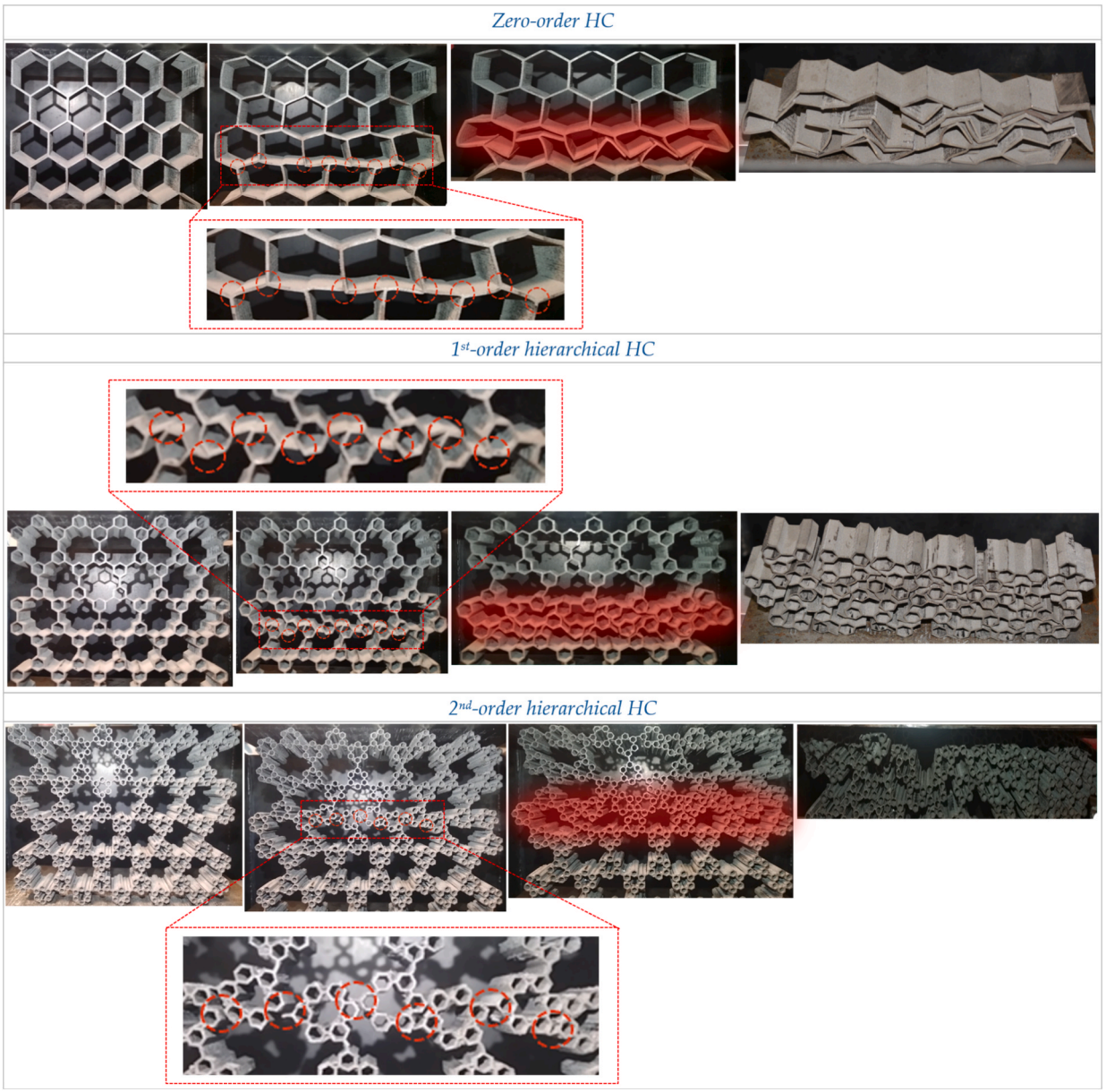


Fig. 17. Evolution of deformation, fracture and bulk sliding in the three levels of hierarchical HCs under y-directional loading.

reflects how the hierarchical design enhances load distribution and energy absorption through progressive failure.

Averaging the load curves, as shown in Fig. 21(d, e, and f), was necessary to account for inconsistencies like misalignments, material imperfections, or manufacturing deviations, which can introduce noise. This process smooths out fluctuations and provides a clearer, more reliable representation of the overall structural behaviour. In contrast, non-averaged curves may reflect irregularities specific to individual tests rather than the inherent material or design behaviour. Averaging highlights consistent trends in load capacity, deformation, and failure mechanisms, offering a more accurate and robust understanding of the structure's performance.

The load bearing capacity of hierarchical HCs was observed to be ranked from highest to lowest from zero-order, 1st-order, and 2nd-order hierarchical HCs, for loading in the *x*- and *y*-directions, separately. Such a ranking could occur because as the hierarchy increases the load paths get more complicated, introducing more possible failure spots and lowering overall load-bearing capacity. Such ranking is not available in literature, which was all found to be focused energy absorption instead [6,31–44,51–53,57,58,67–70]. Ranking the failure loads of three hierarchical HCs in two in-plane directions reveals significant performance differences among the various hierarchical designs. The zero-order HC ($x_{Average}$) has the lowest failure load, not able to sustain higher loads before failure. The zero-order HC ($y_{\text{-Average}}$) performs slightly better but still ranks low compared to HCs of higher hierarchical levels. The 1st-order hierarchical HCs show a notable increase in failure loads, indicating enhanced structural complexity and better stress distribution. The 2nd-order hierarchical HCs rank the highest, featuring advanced designs that maximize load capacity and energy absorption. The observation is based on the overall trend across all samples, and the few instances of lower peak loads do not undermine this general finding. This trend underscores the importance of hierarchical design in enhancing mechanical performance, with each level providing increased resilience and strength. However, as noted previously in this section, the difference in failure loads diminishes with higher hierarchy levels for loading in the two in-plane directions independently, preventing a clear ranking of the 1st-order and 2nd-order hierarchical HCs.

It must also be noted that in this study, the 1st- and 2nd-order

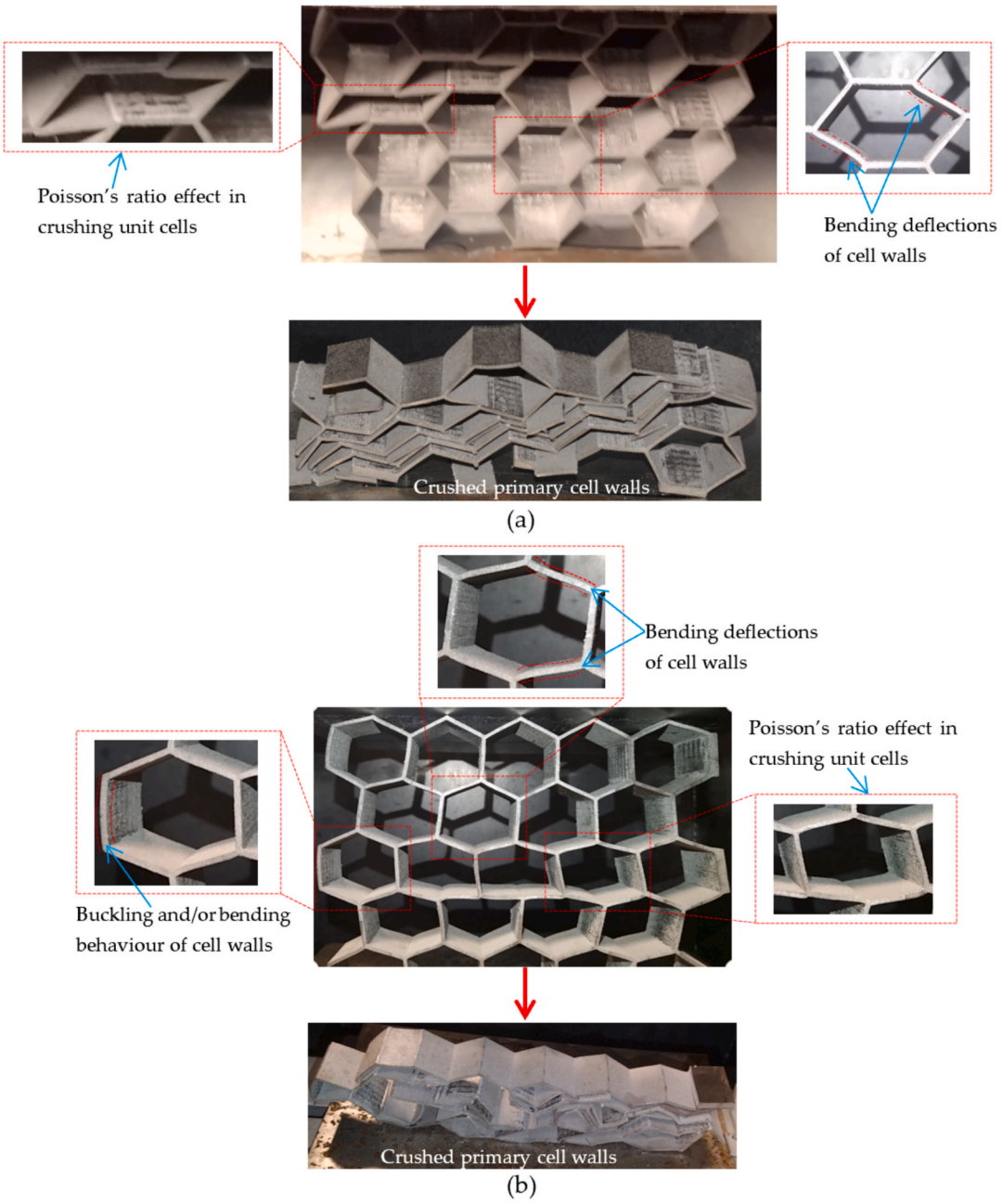


Fig. 18. The deformation trends and levels of crushing till densification of the material for the zero-order HC loaded in the; (a) x-direction and (b) y-direction

hierarchical HCs are crushed only at the first, lowest level of the hierarchy. This implies that if successive crushing events were to occur, higher energy absorption could be achieved due to the increased failure loads at higher hierarchical levels.

Failure as a function of the manufacturing flaws in the cell walls of the structure- The zero-order HC specimens ($x1$ and $x2$), shown in Fig. 21(a), exhibit clear differences in load peaks after the first peak, with $x2$ showing significantly lower peaks. This difference simply put is related to the failure along an inclined line as observed previously, where the cell walls separation completed before complete crushing. This might denote the presence of flaws in the cell walls at the points where separation occurred and could denote poor sintering at the points. Fig. 22 compares the load curves for both HCs in the x-direction, with x2 corresponding to the images in the figure.

Specific energy absorption (SEA) in hierarchical honeycombs – The bar chart in Fig. 23 presents a comparison of *SEA* for zero-order, 1st-order, and 2nd-order hierarchical HCs in both x- and y- directions of loading.

A clear trend emerges showing that *SEA* decreases as the order of hierarchy increases, regardless of the direction of loading. This reduction in *SEA* with increasing hierarchy may initially appear counterintuitive, particularly given that hierarchical structures are typically engineered for enhanced mechanical performance [70,71]. However, the observed trend is directly tied to the shear type of failure at an inclination to the axis of loading of the first hierarchical level and the lack of activation of failure of the higher 1st –and 2nd – order hierarchies Thus the higher-order, more robust structural levels that define hierarchical HCs were not activated in the energy absorption process. Since the failure of upper hierarchical levels typically occurs at higher loads, they possess greater potential for absorbing energy, especially in staged or progressive collapse scenarios. Thus, the current results in which the higher orders were not activated underrepresent the full energy

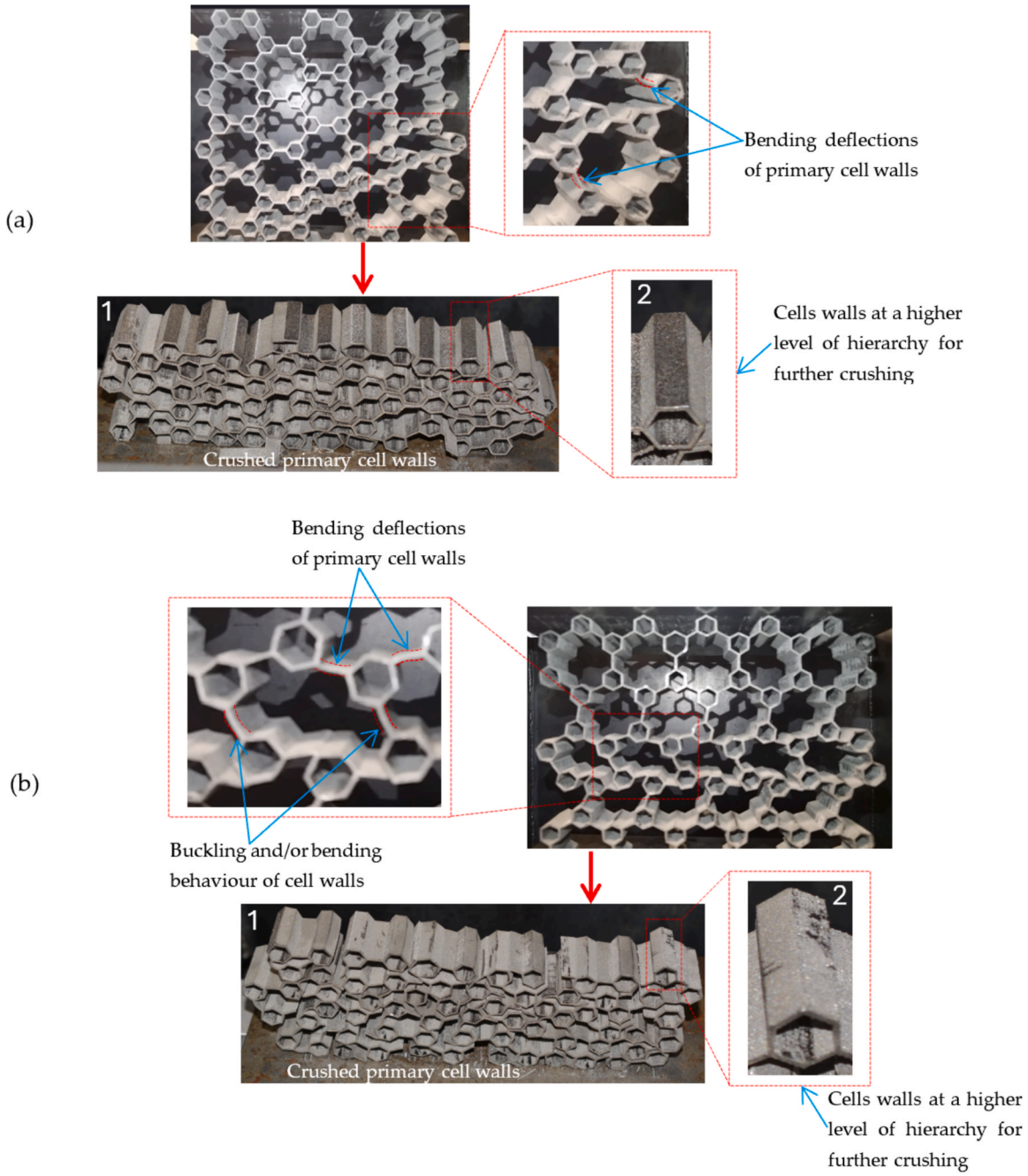


Fig. 19. The deformation trends and levels of crushing before densification of the material for the 1st-order hierarchical HC loaded in the; (a) x-direction and (b) y-direction

absorption capability of hierarchical HCs. In impact protection systems, biomedical implants, or crashworthy components, where progressive failure mechanisms or multi-stage deformation can be triggered through different levels of hierarchy, these structures are expected to outperform zero-order HCs significantly.

3.3. Expanded discussion with Gibson-Ashby and hierarchical beam theory comparisons

The observed trends in failure loads and deformation mechanisms for hierarchical HCs under *x*- and *y*-directional crushing is partly rationalised using established theoretical models for cellular solids. In particular, *Gibson and Ashby's model* provides a foundational basis for understanding mechanical behaviour of cellular structures, including bending-dominated and stretching-dominated architectures [70]. Gibson–Ashby models predict that for open-cell bending-dominated structures, such as the zero-order HCs presented here, the crushing strength (σ^*) scales with relative density (ρ^*) as follows:

$$\sigma^* \propto \sigma_s \left(\frac{\rho^*}{\rho_s}\right)^{3/2} \tag{4}$$

where:

- σ_s is the yield strength of the solid material (Ti6Al4V ELI),
- ρ^* is the density of the cellular structure,
- ρ_s is the density of the solid.

Given the thin-walled construction and the predominance of bending

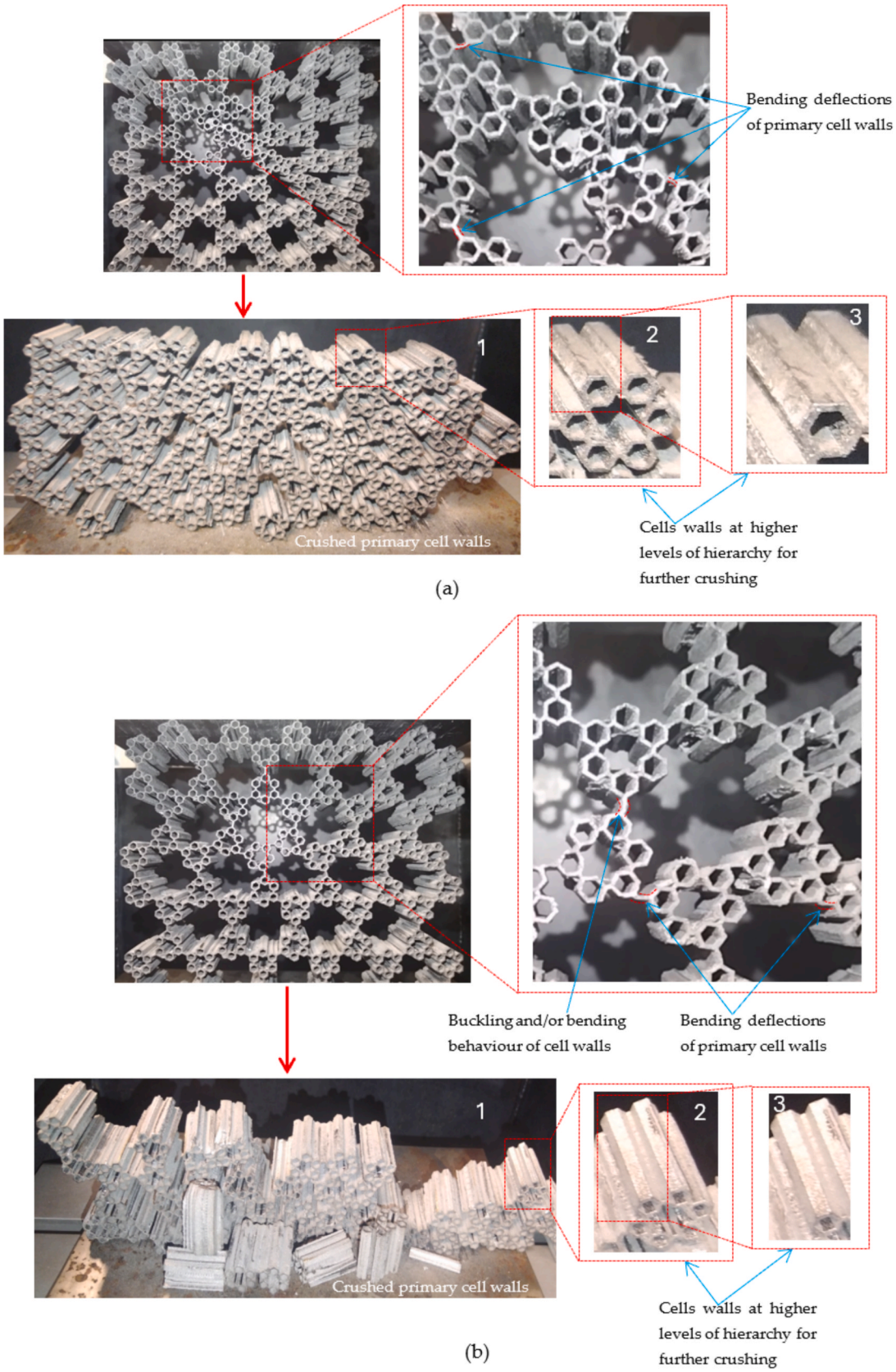


Fig. 20. The deformation trends and levels of crushing before densification of the material for the 2nd-order hierarchical HC loaded in the; (a) x-direction and (b) y-direction

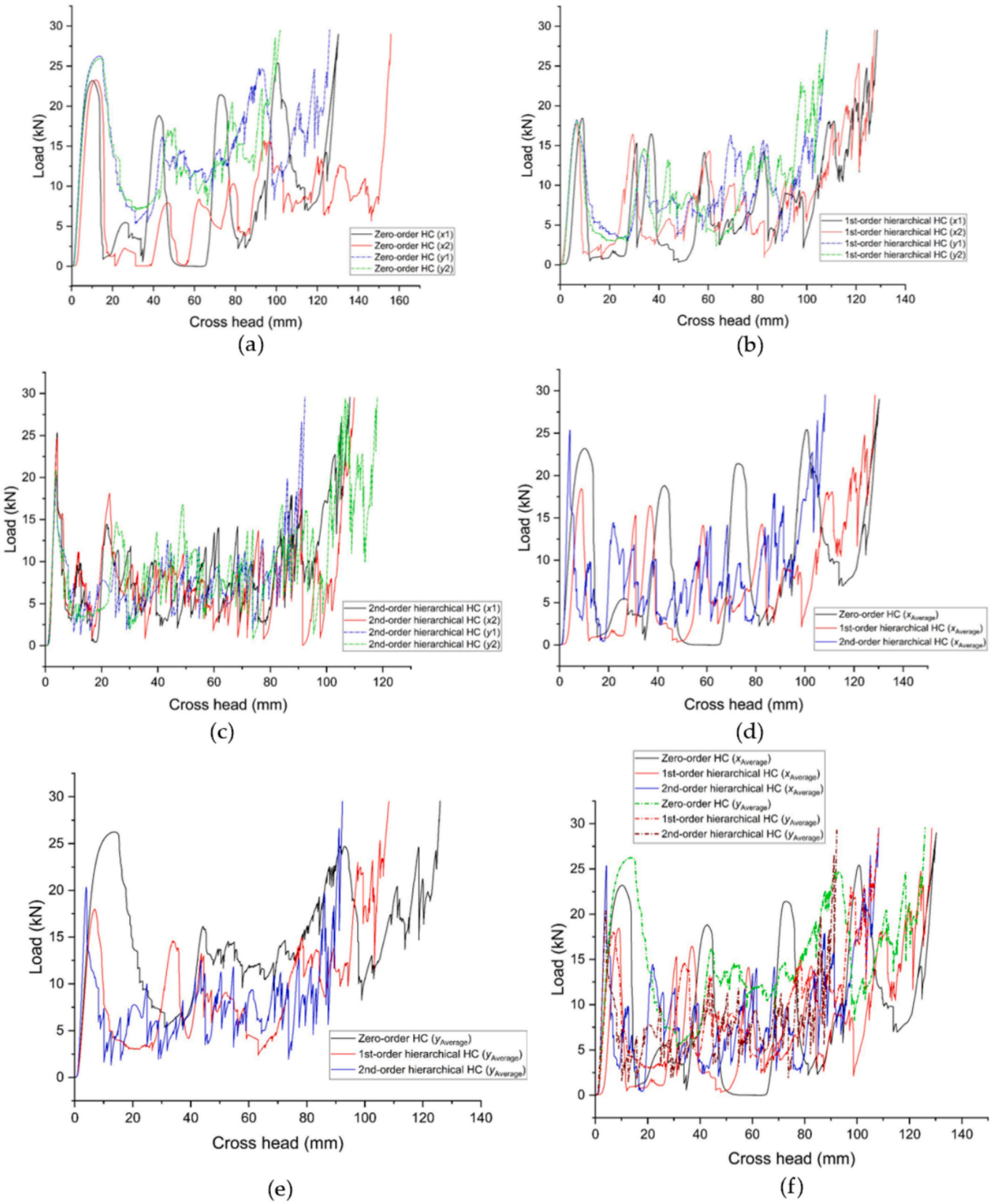


Fig. 21. Load-displacement curves for crushing three levels of hierarchical HCs along the two x and y in-plane directions.

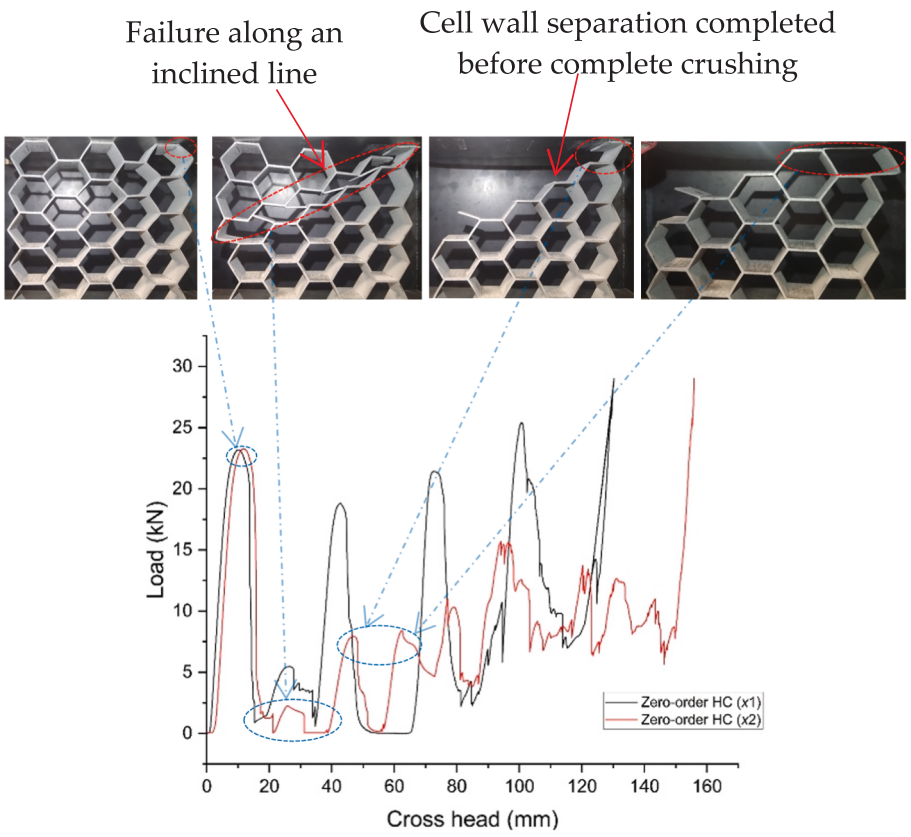


Fig. 22. Specimen failure as a function of the manufacturing flaws in the cell walls.

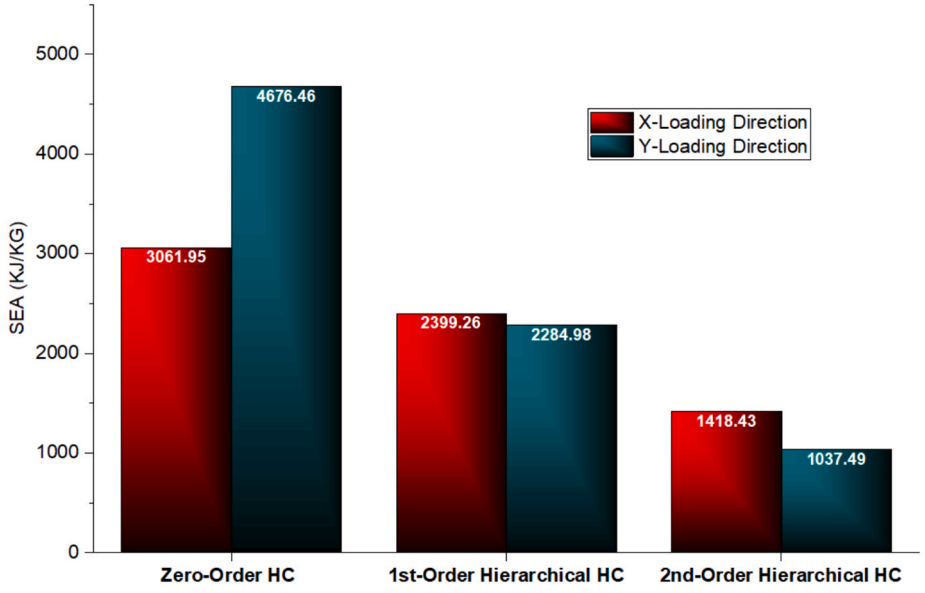


Fig. 23. Specific energy absorption comparison for different levels of hierarchical HCs under x- and y-directional loading.

and buckling observed in the deformation (particularly under *y*-directional loading), the structures conform well to this bending-dominated scaling regime. The decrease in load-bearing capacity with increasing order of hierarchy can be attributed to the increase in the number of joints and smaller-scale members, which decrease the effective relative density and introduce more potential failure points, consistent with the $(\rho^*/\rho_s)^{3/2}$ scaling [70,71]. However, these classical models do not fully capture the tiered progressive collapse observed in higher-order hierarchical HCs, where failure proceeds through localised bending, fracture at vertices, and sliding followed by densification at each level of hierarchy. To better interpret this behaviour, hierarchical beam theories offer a more appropriate framework.

Comparison with hierarchical beam theories. Recent work in hierarchical lattice theory suggests that mechanical strength and stiffness can scale sub-linearly or super-linearly depending on the hierarchy's geometric construction and connectivity [72,73]. Hierarchical beams

can distribute stress more efficiently, delaying localised failure, and increasing the energy absorption capability by activating additional deformation modes at each level.

In the current study, the failure load hierarchy (zero < 1st < 2nd order hierarchical HCs), alongside the observed cyclic increase in peak loads after initial fractures (as shown in Fig. 21), aligns well with hierarchical load redistribution models. These models predict that higher-order structures can compartmentalise failure, allowing undamaged regions to maintain load-bearing capacity even as localised fractures occur, effectively blunting the propagation of catastrophic failure. This progressive load redistribution is not predicted by the original Gibson-Ashby models but has been verified in multiscale beam lattice simulations, where self-similar, fractal-like geometries exhibit enhanced damage tolerance and energy absorption [74]. Moreover, the reduction in directional sensitivity with increasing hierarchy, evidenced by more similar load curves for *x*- and *y*-loading in the 1st- and 2nd-order hierarchical HCs, is another signature of hierarchical homogenisation. At higher orders, the geometric anisotropy is statistically averaged out across the multiple layers of unit cells, leading to more quasi-isotropic behaviour, as suggested in multiscale homogenisation theories.

Poisson's ratio effect and failure loads. The observed reduction of the Poisson's effect in higher hierarchical orders also aligns with Gibson-Ashby predictions and hierarchical beam mechanics. In low-order bending-dominated structures, axial compression results in lateral expansion, resulting in noticeable Poisson's effects. In contrast, in hierarchical systems, load paths become more distributed, and local deformations no longer propagate uniformly across the sample, leading to a muted macroscopic Poisson response [75].

Table 2 shows the summary of theoretical comparison implications for investigating hierarchical HCs under compression loading.

While the Gibson–Ashby framework effectively describes the basic mechanical behaviour of bending-dominated cellular solids like zero-order HCs, it does not account for the progressive collapse and load redistribution mechanisms observed in hierarchical designs. Hierarchical beam theory and multiscale modelling offer a more suitable lens to interpret the experimental phenomena presented, especially the tiered failure, cyclic load recovery, and directional homogenisation. These insights highlight the necessity of extending traditional cellular solid models to encompass hierarchical mechanical principles, particularly for applications involving graded energy absorption, programmable failure, and multi-stage deformation.

Existing theoretical derivation of relative density for hierarchical HCs and comparison to current experimental failure loads. For a regular hexagonal HC made of thin cell walls:

$$\rho^* = \frac{2t}{\sqrt{3}l} \tag{5}$$

Table 2
Summary of theoretical comparison implications.

Observation from Study	Explained by Gibson–Ashby?	Explained by Hierarchical Beam Theories?
Bending and buckling in thin walls	✔ Yes	✔ Yes
Failure at wall vertices due to stress concentration	✔ Yes	✔ Yes
Progressive failure across hierarchical levels	✘ No	✔ Yes
Increasing load cycles and redistribution of stress	✘ No	✔ Yes
Reduced directional sensitivity at higher hierarchies	✘ No	✔ Yes
Decreasing Poisson's ratio with hierarchy	Partial	✔ Yes
Ranking of failure loads across hierarchy	✘ No (focuses on energy absorption)	✔ Emerging topic

- t: wall thickness
- l: cell edge length (length of one wall)

This assumes vertical and angled walls with uniform thickness and isotropic distribution. The first level of hierarchy replaces the solid walls of the zero-order HC with smaller hexagonal sub-cells (each of the same form). Assuming self-similarity and uniform wall thickness:

$$\rho_1^* = \rho_1^* \bullet \frac{2t}{\sqrt{3}l_1} = \left(\frac{2t}{\sqrt{3}\,l_0}\right) \bullet \left(\frac{2t}{\sqrt{3}\,l_1}\right) = \frac{4t^2}{3l_0l_1} \tag{6}$$

- l_1: length of smaller unit cell walls (1st hierarchy)
- l_0: size of the initial macro-cell wall

Substitute the 1st –order sub-cell walls with a second level of sub-sub-cells:

$$\rho_2^* = \rho_1^* \bullet \frac{2t}{\sqrt{3}l_2} = \left(\frac{4t^2}{3l_0l_1}\right) \bullet \left(\frac{2t}{\sqrt{3}\,l_2}\right) = \frac{8t^3}{3\sqrt{3}l_0l_1l_2} \tag{7}$$

And so on for higher orders:

$$\rho_n^* = \rho_s \bullet C \bullet \left(\frac{t}{l_0}\right)^n \tag{8}$$

where C is a geometric constant depending on the topology. The theoretical predictions (from mechanics models) are now compared with experimental failure loads from the crushing tests. In HCs where deformation is dominated by bending:

$$\sigma_{fail}^* = C_1 \bullet E_s\left(\frac{t}{l}\right)^3 = C_1 \bullet E_s(\rho^*)^{3/2} \tag{9}$$

where C_1 is an empirical geometric constant (~0.3 to 0.5 depending on cell orientation and loading direction). For thin-walled structures under axial compression, buckling can dominate:

$$\sigma_{buckling}^* = C_2 \bullet E_s\left(\frac{t}{l}\right)^2 = C_2 \bullet E_s(\rho^*)^{4/3} \tag{10}$$

where C_1 is an empirical geometric constant as well. Table 3 shows the comparison of the theoretical predictions to the experimental load curves refenced in Fig. 20 of the current study.

It is evident from the information contained in the preceding table that the failure loads increase with increasing hierarchical order. This can be attributed to the enhanced resistance to deformation with increasing hierarchy, an observation consistent with predictions from the Gibson–Ashby scaling laws [71]. Furthermore, anisotropy has been observed in literature to decrease with increasing hierarchy; experimental results reveal that directional sensitivity is more pronounced in zero-order HC s compared to 2nd-order structures. This trend corresponds to the increased geometric symmetry and the more uniform load distribution characteristic of higher-order hierarchies [70,71]. The progressive crushing behaviour, evident from the sequential drops and rises in the load–displacement curves, reflects the multi-stage deformation mechanism predicted by hierarchical design models, wherein lower-level substructures collapse prior to those in higher levels. Failure loads increase due to progressive and distributed deformation, matching well with the theory predicting failure as a function of the expression ($\propto (\rho^*)^{3/2}$) shown in Table 3 [70].

4. Challenges and the way forward in updating design concepts and experimental tests for additively-produced hierarchical lattice parts

Mechanically removing scaffolds is labor-intensive and can result in delamination, surface damage and therefore, significance inaccuracies

Table 3
Comparison of the theoretical models to the experimental load curves.

Hierarchy Level	Direction	Failure Mechanism	Relative Density ρ^*	Predicted σ^*_{fail}	Experimental Peak Load Trend
Zero-order	*x*	Bending/Sliding	$\sim \rho_0$	$\sim (\rho_0)^{3/2}$	Lowest
Zero-order	*y*	Buckling	$\sim \rho_0$	$\sim (\rho_0)^{4/3}$	Slightly higher than *x*
1st-order	*x and y*	Bending	$\sim \rho_1$	$\sim (\rho_1)^{3/2}$	Higher than 0th
2nd-order	*x and y*	Progressive Bending	$\sim \rho_2$	$\sim (\rho_2)^{3/2}$	Highest, more stable

particularly in complex designs such as hierarchical lattice structures [63,67]. In addition, the method of removing scaffolding is laborious and slow, and causes delays in production, which is a serious problem particularly in sectors such as aerospace where delivery on schedule is crucial [63]. The challenge thus is finding faster and effective removal procedures without sacrificing the quality or safety of printed complex metallic parts [15,71,76]. Develop robotic systems equipped with machine learning and vision-based pattern recognition to accurately identify and remove scaffolds from complex lattice structures, reducing labor intensity and improving precision in scaffold removal. Investigation should be carried out to produce scaffolds that are easy to remove, with greater accuracy, and that require minimal human labour. Develop scaffolds from materials that dissolve or change phase when triggered by specific stimuli (e.g., heat, solvents, or magnetic fields). This method allows for non-invasive removal, reducing the risk of delamination and surface damage. Explore material-based design strategies that reduce the need for scaffolding by optimising mechanical properties and weight distribution in complex parts during AM. Hierarchical lattices with graded densities can offer inherent support, minimising dependence on external scaffolds.

The damage models used today for analysing the crushing behaviour for both regular and hierarchical lattice systems are lacking because their predictions are constrained to the first load drop. Powerful and proven dimensional analysis concepts, including the Buckingham Pi theorem [77], must be applied in the development of upgraded damage models that could add to the core aspect in the study of damage in complicated structures. These upgraded damage models should integrate micromechanical mechanisms for damage to accurately capture progressive failure at various scales within hierarchical structures. The use of continuum damage mechanics strategies that take account of damage accumulation and its effect on the properties of materials should be considered as well. Furthermore, it should interact with cohesive zone models to mimic crack initiation and propagation, thus providing a more accurate representation of post-peak behaviour.

Comparing the current physical experiments of regular hierarchical HCs with numerical models of topology-optimised hierarchical HCs is essential for validating performance improvements from optimisation strategies. Regular models offer foundational insights into structural behaviour, while topology optimisation enhances effectiveness, reduces weight, and increases robustness by tailoring material distribution to specific loading conditions. This comparison allows researchers to assess the impact of optimisation on strength, stiffness, and failure modes, ensuring that theoretical benefits translate into tangible physical advantages, thereby enhancing the entire design process.

5. Conclusions

This study used the DMLS technique to investigate the quasi-static crushing behavior of Ti6Al4V(ELI) hierarchical honeycomb structures. The findings provide new insights into their effectiveness under quasi-static compression and address questions about mechanical property rankings. From the experimental analysis, the following conclusions were drawn:

- The observed surface roughness deviations in DMLS-produced specimens indicate potential inconsistencies in the AM process, which could influence the mechanical performance and reliability of the final parts. Comparisons of three orders of hierarchy of HCs revealed that the average surface roughness (*Ra*) increased with increasing hierarchy. The *Ra* for each hierarchical level in HCs also showed lower readings for the top flat surfaces than side inclined surfaces. Simple bead blasting led to a significant improvement of the average surface roughness.
- The walls of the hierarchical structures were observed to deform primarily through beam bending. Buckling deformation was observed to be pronounced for *y*-direction loading.
- The drop of loads after attaining peaks in an oscillatory manner was thought to be a results of fracture at the vertices of walls, following initial primarily bending and/or buckling as the case was.
- The hierarchical HCs collapsed under compression loads via bending and/or buckling, Poisson's ration lateral expansion and finally, sliding along an inclined line and horizontally, for x-and y-direction loading, respectively.
- Crushing was observed to occur sequentially, starting with the lowest order of hierarchy and moving up to the highest order.
- Zero-order HCs had the lowest failure load, while first-order HCs showed an increase. Second-order HCs exhibited the highest failure loads. This observation is based on observed overall trends and the few second-order peak loads that are lower than those of the first-order do not detract from this conclusion.
- Variations in failure loads decreased with higher hierarchy levels, making it challenging to rank 1st- and 2nd-order HCs based on loading directions.
- The zero-order HC specimens ($x1$ and $x2$) had notable load peak differences after the first one, with $x2$ having substantially lower peaks, most likely due to failure along an inclined line, implying flaws or poor sintering at separation points of the cell walls.
- Though the observed decrease in *SEA* with increasing hierarchy suggests reduced performance, this is primarily due to the limited activation of only the lowest hierarchical level during crushing. Higher-order hierarchical features, which remain unengaged under these conditions, possess untapped energy absorption capacity. Activation of these levels, through increased deformation is expected to significantly enhance the overall *SEA* response.

CRediT authorship contribution statement

M.I. Chibinyani: Writing – review & editing, Writing – original draft, Visualization, Validation, Project administration, Methodology, Investigation, Formal analysis, Data curation, Conceptualization. **T.C. Dzogbewu:** Writing – review & editing, Visualization, Validation, Supervision, Project administration, Methodology, Funding acquisition. **M. Maringa:** Writing – review & editing, Visualization, Validation, Supervision, Project administration, Methodology, Funding acquisition. **A.M. Muiruri:** Writing – review & editing, Visualization, Validation, Supervision, Project administration.

Declaration of competing interest

The authors declare that they have no known competing financial interests or personal relationships that could have appeared to influence the work reported in this paper.

Acknowledgements

Funding: This work is based on research supported by the South African Research Chairs Initiative of the Department of Science and Technology, and the National Research Foundation of South Africa (Grant No. 97994), and the Collaborative Program in Additive Manufacturing (Contract No. CSIR-NLC-CPAM-21-MOA-CUT-03).

Data availability

The data that support the findings of this study are available from the corresponding author, [M.I.C], upon reasonable request.

References

[1] F.N. Habib, P. Iovenitti, S.H. Masood, M. Nikzad, Fabrication of polymeric lattice structures for optimum energy absorption using Multi Jet Fusion technology, Mater. Des. 155 (2018) 86–98.
[2] S.H. Siddique, P.J. Hazell, H. Wang, J.P. Escobedo, A.A. Ameri, Lessons from nature: 3D printed bio-inspired porous structures for impact energy absorption–A review, Addit. Manuf. 58 (2022) 103051.
[3] C.W. Isaac, F. Duddeck, Current trends in additively manufactured (3D printed) energy absorbing structures for crashworthiness application–a review, Virtual Phys. Prototyp. 17 (4) (2022) 1058–1101.
[4] L. Greco, F. Buccino, Z. Xu, L. Vergani, F. Berto, M. Guagliano, et al., Design and analysis of energy absorbent bioinspired lattice structures, J. Bionic Eng. 20 (4) (2023) 1670–1686.
[5] D. Ramakrishna, G. Bala Murali, Bio-inspired 3D-printed lattice structures for energy absorption applications: A review, Proc. Inst. Mech. Eng., Part L: J. Mater.: Des. Appl. 237 (3) (2023) 503–542.
[6] H. Mohammadi, Z. Ahmad, M. Petrů, S.A. Mazlan, M.A.F. Johari, H. Hatami, S.S. R. Koloor, An insight from nature: honeycomb pattern in advanced structural design for impact energy absorption, J. Mater. Res. Technol. 22 (2023) 2862–2887.
[7] Y. Yang, X. Song, X. Li, Z. Chen, C. Zhou, Q. Zhou, Y. Chen, Recent progress in biomimetic additive manufacturing technology: from materials to functional structures, Adv. Mater. 30 (36) (2018) 1706539.
[8] N.D. Dejene, H.G. Lemu, Current status and challenges of powder bed fusion-based metal additive manufacturing: literature review, Metals 13 (2) (2023) 424.
[9] A.A. Ahmed, M.A. Nazzal, B.M. Darras, A. Eltaggaz, I.M. Deiab, Comparative sustainability assessment of powder bed fusion and solid-state additive manufacturing processes: The case of direct metal laser sintering versus additive friction stir deposition, Sustain. Mater. Technol. 39 (2024) e00858.
[10] A. Jiménez, P. Bidare, H. Hassanin, F. Tarlochan, S. Dimov, K. Essa, Powder-based laser hybrid additive manufacturing of metals: a review, Int. J. Adv. Manuf. Technol. 114 (2021) 63–96.
[11] Y. Zhang, S. Yang, Y.F. Zhao, Manufacturability analysis of metal laser-based powder bed fusion additive manufacturing—a survey, Int. J. Adv. Manuf. Technol. 110 (2020) 57–78.
[12] V. Madhavadas, D. Srivastava, U. Chadha, S.A. Raj, M.T.H. Sultan, F.S. Shahar, A. U.M. Shah, A review on metal additive manufacturing for intricately shaped aerospace components, CIRP J. Manuf. Sci. Technol. 39 (2022) 18–36.
[13] G. Liu, X. Zhang, X. Chen, Y. He, L. Cheng, M. Huo, et al., Additive manufacturing of structural materials, Mater. Sci. Eng.: R: Rep. 145 (2021) 100596.
[14] S. Hasanov, S. Alkunte, M. Rajeshirke, A. Gupta, O. Huseynov, I. Fidan, et al., Review on additive manufacturing of multi-material parts: Progress and challenges, J. Manuf. Mater. Process. 6 (1) (2021) 4.
[15] T.D. Ngo, A. Kashani, G. Imbalzano, K.T. Nguyen, D. Hui, Additive manufacturing (3D printing): A review of materials, methods, applications and challenges, Compos. Part B: Eng. 143 (2018) 172–196.
[16] G. Suresh, M.R. Ramesh, M.S. Srinath, Surface engineered titanium alloys for biomedical, automotive, and aerospace applications, in: Advances in Processing of Lightweight Metal Alloys and Composites: Microstructural Characterization and Property Correlation, Springer Nature Singapore, Singapore, 2022, pp. 89–102.
[17] S.A. Salihu, Y.I. Suleiman, A.I. Eyinavi, Classification, Properties and Applications of titanium and its alloys used in automotive industry—A Review, Am. J. Eng. Res 4 (2019) 92–98.
[18] N. Singh, P. Hameed, R. Ummethala, G. Manivasagam, K.G. Prashanth, J. Eckert, Selective laser manufacturing of Ti-based alloys and composites: Impact of process parameters, application trends, and future prospects, Mater. Today Adv. 8 (2020) 100097.
[19] J.D. Avila, S. Bose, A. Bandyopadhyay, Additive manufacturing of titanium and titanium alloys for biomedical applications, in: Titanium in Medical and Dental Applications, Woodhead Publishing, 2018, pp. 325–343.
[20] V. Dhinakaran, M. Varsha Shree, T. Jagadeesha, M. Swapna Sai, Additive manufacturing: technology, materials and applications in aerospace, Light Weight Mater.: Process. Character. (2022) 1–22.
[21] A.M. Khorasani, M. Goldberg, E.H. Doeven, G. Littlefair, Titanium in biomedical applications—properties and fabrication: a review, J. Biomater. Tissue Eng. 5 (8) (2015) 593–619.
[22] T.S. Tshephe, S.O. Akinwamide, E. Olevsky, P.A. Olubambi, Additive manufacturing of titanium-based alloys-A review of methods, properties, challenges, and prospects, Heliyon 8 (3) (2022).
[23] D. Salas, D. Ebeperi, M. Elverud, R. Arróyave, R.J. Malak, I. Karaman, Embedding hidden information in additively manufactured metals via magnetic property grading for traceability, Addit. Manuf. 60 (2022) 103261.
[24] N. Hou, M. Wang, B. Wang, Y. Zheng, S. Zhou, C. Song, Fundamental functions of physical and chemical principles in the polishing of titanium alloys: mechanisms and problems, Int. J. Adv. Manuf. Technol. (2021) 1–19.
[25] H.A. Colorado, C.A. Cardenas, E.I. Gutierrez-Velazquez, J.P. Escobedo, S. N. Monteiro, Additive manufacturing in armor and military applications: research, materials, processing technologies, perspectives, and challenges, J. Mater. Res. Technol. (2023).
[26] D.E. Mouzakis, Advanced technologies in manufacturing 3D-layered structures for defense and aerospace, Laminat.-Theory Appl. 74331 (2018).
[27] S. Rouf, A. Malik, N. Singh, A. Raina, N. Naveed, M.I.H. Siddiqui, M.I.U. Haq, Additive manufacturing technologies: Industrial and medical applications, Sustainable Oper. Comput. 3 (2022) 258–274.
[28] M. Mani, P. Witherell, H. Jee, Design rules for additive manufacturing: A categorization. International Design Engineering Technical Conferences and Computers and Information in Engineering Conference, American Society of Mechanical Engineers, 2017.
[29] A. Makes, A.A.M.S. Collaborative, Standardization roadmap for additive manufacturing, Public Draft. (2017).
[30] R. Russell, D. Wells, J. Waller, B. Poorganji, E. Ott, T. Nakagawa, et al., Qualification and certification of metal additive manufactured hardware for aerospace applications, Additive Manuf. Aerospace Ind. (2019) 33–66.
[31] N. Jaiswal, U. Bharti, A. Yadav, M. Srivastava, S. Rathee, Static structural and thermal analysis of honeycomb structure fabricated by friction stir processing route: A case study, Friction Stir Weld. Process.: Fundament. Advancem. (2024) 283–292.
[32] K.N. Islam, J. Hildenbrand, M.M. Hossain, Life cycle impacts of three-way ceramic honeycomb catalytic converter in terms of disability adjusted life year, J. Clean. Prod. 182 (2018) 600–615.
[33] D.N. Tsinoglou, P.D. Eggenschwiler, T. Thurnheer, P. Hofer, A simplified model for natural-gas vehicle catalysts with honeycomb and foam substrates, Proc. Inst. Mech. Eng., Part D: J. Automobile Eng. 223 (6) (2009) 819–834.
[34] B. Hu, J. Yao, N. An, H. Mi, X. Bai, Numerical investigation on the effects of HC geometry on the flow and heat transfer in the disk cavity system at the turbine vane root, Appl. Therm. Eng. 230 (2023) 120794.
[35] A. Munir, Microwave radar absorbing properties of multiwalled carbon nanotubes polymer composites: a review, Adv. Polym. Tech. 36 (3) (2017) 362–370.
[36] Y. Zhang, L. Yang, Y. Tian, L. Li, J. Li, T. Qiu, et al., Honeycomb hard carbon derived from carbon quantum dots as anode material for K-ion batteries, Mater. Chem. Phys. 229 (2019) 303–309.
[37] M. Sajjad, W. Lu, Honeycomb-based heterostructures: An emerging platform for advanced energy applications: A review on energy systems, Electrochem. Sci. Adv. 2 (5) (2022) e202100075.
[38] H. Dai, W. Dai, Z. Hu, W. Zhang, G. Zhang, R. Guo, Advanced composites inspired by biological structures and functions in nature: architecture design, strengthening mechanisms, and mechanical-functional responses, Adv. Sci. 10 (14) (2023) 2207192.
[39] A. Hönig, W.J. Stronge, In-plane dynamic crushing of honeycomb. Part I: crush band initiation and wave trapping, Int. J. Mech. Sci. 44 (8) (2002) 1665–1696.
[40] S.D. Papka, S. Kyriakides, Experiments and full-scale numerical simulations of in-plane crushing of a honeycomb, Acta Mater. 46 (8) (1998) 2765–2776.
[41] L.L. Hu, T.X. Yu, Dynamic crushing strength of hexagonal honeycombs, Int. J. Impact Eng 37 (5) (2010) 467–474.
[42] S.D. Papka, S. Kyriakides, In-plane crushing of a polycarbonate honeycomb, Int. J. Solids Struct. 35 (3–4) (1998) 239–267.
[43] S.A. Galehdari, M. Kadkhodayan, S. Hadidi-Moud, Analytical, experimental and numerical study of a graded honeycomb structure under in-plane impact load with low velocity, Int. J. Crashworthiness 20 (4) (2015) 387–400.
[44] S.D. Papka, S. Kyriakides, Biaxial crushing of honeycombs: —Part 1: Experiments, Int. J. Solids Struct. 36 (29) (1999) 4367–4396.
[45] Q. Zhang, X. Yang, P. Li, G. Huang, S. Feng, C. Shen, et al., Bioinspired engineering of honeycomb structure–Using nature to inspire human innovation, Prog. Mater Sci. 74 (2015) 332–400.
[46] S. Akdag, M. Karakus, G.D. Nguyen, A. Taheri, Strain burst vulnerability criterion based on energy-release rate, Eng. Fract. Mech. 237 (2020) 107232.
[47] B.S. Lazarus, A. Velasco-Hogan, T. Gómez-del Río, M.A. Meyers, I. Jasiuk, A review of impact resistant biological and bioinspired materials and structures, J. Mater. Res. Technol. 9 (6) (2020) 15705–15738.
[48] H. Mozafari, H. Molatefi, V. Crupi, G. Epasto, E. Guglielmino, In plane compressive response and crushing of foam filled aluminum honeycombs, J. Compos. Mater. 49 (26) (2015) 3215–3228.
[49] Y. Zhou, Y. Pan, Q. Gao, B. Sun, In-plane quasi-static crushing behaviors of a novel reentrant combined-wall honeycomb, J. Appl. Mech. 90 (5) (2023) 051002.
[50] N.K. Choudhry, B. Panda, S. Kumar, In-plane energy absorption characteristics of a modified re-entrant auxetic structure fabricated via 3D printing, Compos. Part B: Eng. 228 (2022) 109437.
[51] C. Qi, F. Jiang, S. Yang, Advanced honeycomb designs for improving mechanical properties: A review, Compos. Part: B Eng. 227 (2021) 109393.
[52] Z. Wang, Recent advances in novel metallic honeycomb structure, Compos. Part: B Eng. 166 (2019) 731–741.
[53] W.H. Choi, C.G. Kim, Broadband microwave-absorbing honeycomb structure with novel design concept, Compos. Part: B Eng. 83 (2015) 14–20.
[54] X. Wei, J. Xiong, J. Wang, W. Xu, New advances in fiber-reinforced composite honeycomb materials, Sci. China Technol. Sci. 63 (8) (2020) 1348–1370.

[55] R. Oftadeh, B. Haghpanah, D. Vella, A. Boudaoud, A. Vaziri, Optimal fractal-like hierarchical honeycombs, Phys. Rev. Lett. 113 (10) (2014) 104301.
[56] R. Oftadeh, B. Haghpanah, J. Papadopoulos, A.M.S. Hamouda, H. Nayeb-Hashemi, A. Vaziri, Mechanics of anisotropic hierarchical honeycombs, Int. J. Mech. Sci. 81 (2014) 126–136.
[57] Y. Zhang, Y. Lin, Y. Li, X. Li, 3D printed self-similar AlSi10Mg alloy hierarchical honeycomb architectures under in-plane large deformation, Thin-Walled Struct. 164 (2021) 107795.
[58] Y. Zhang, Y. Lin, X. Li, Plastic crushing failure of bio-inspired cellular hierarchical topological sandwich core, Materials 14 (17) (2021) 5040.
[59] Y. Chen, H. Hu, In-plane elasticity of regular hexagonal honeycombs with three different joints: A comparative study, Mech. Mater. 148 (2020) 103496.
[60] A. Ajdari, B.H. Jahromi, J. Papadopoulos, H. Nayeb-Hashemi, A. Vaziri, Hierarchical honeycombs with tailorable properties, Int. J. Solids Struct. 49 (11–12) (2012) 1413–1419.
[61] A. Muiruri, M. Maringa, W. du Preez, Quasi-static mechanical properties of post-processed laser powder bed fusion Ti6Al4V (ELI) parts under compressive loading, Appl. Sci. 12 (19) (2022) 9552.
[62] L. Mugwagwa, D. Dimitrov, S. Matope, R. Muvunzi, Residual stresses and distortions in selective laser melting-a review, in: Proceedings of the 17th Rapid Product Development Association of South Africa, Vanderbijlpark, South Africa, 2016, pp. 2–4.
[63] K. Ishfaq, M. Abdullah, M.A. Mahmood, A state-of-the-art direct metal laser sintering of Ti6Al4V and AlSi10Mg alloys: Surface roughness, tensile strength, fatigue strength and microstructure, Opt. Laser Technol. 143 (2021) 107366.
[64] A. Muiruri, M. Maringa, W. Du Preez, L. Masu, Effects of stress-relieving heat treatment on impact toughness of direct metal laser sintering (DMLS)-produced Ti6Al4V (ELI) parts, JOM 72 (3) (2020) 1175–1185.
[65] L.B. Malefane, W.B. Du Preez, M. Maringa, A. Du Plessis, Tensile and high cycle fatigue properties of annealed Ti6Al4V (ELI) specimens produced by direct metal laser sintering, S. Afr. J. Ind. Eng. 29 (3) (2018) 299–311.
[66] B. Fotovvati, E. Asadi, Size effects on geometrical accuracy for additive manufacturing of Ti-6Al-4V ELI parts, Int. J. Adv. Manuf. Technol. 104 (2019) 2951–2959.
[67] S.R. Narasimharaju, W. Liu, W. Zeng, T.L. See, P. Scott, X. Jiang, S. Lou, Surface texture characterization of metal selective laser melted part with varying surface inclinations, J. Tribol. 143 (5) (2021) 051106.
[68] N. Tepylo, X. Huang, P.C. Patnaik, Laser-based additive manufacturing technologies for aerospace applications, Adv. Eng. Mater. 21 (11) (2019) 1900617.
[69] I. Yadroitsev, P. Bertrand, I. Smurov, Parametric analysis of the selective laser melting process, Appl. Surf. Sci. 253 (19) (2007) 8064–8069.
[70] I.J. Gibson, M.F. Ashby, The mechanics of three-dimensional cellular materials, Proc. Roy. Soc. London. A. Mathe. Phys. Sci. 382 (1782) (1982) 43–59.
[71] H. Zhong, T. Song, C. Li, R. Das, J. Gu, M. Qian, The Gibson-Ashby model for additively manufactured metal lattice materials: Its theoretical basis, limitations and new insights from remedies, Curr. Opin. Solid State Mater. Sci. 27 (3) (2023) 101081.
[72] T.A. Schaedler, A.J. Jacobsen, A. Torrents, A.E. Sorensen, J. Lian, J.R. Greer, W. B. Carter, Ultralight metallic microlattices, Science 334 (6058) (2011) 962–965.
[73] H.K. Zhang, W.J. Wu, Z. Kang, X.Q. Feng, Topology optimization method for the design of bioinspired self-similar hierarchical microstructures, Comput. Methods Appl. Mech. Eng. 372 (2020) 113399.
[74] R. Lakes, Materials with structural hierarchy, Nature 361 (6412) (1993) 511–515.
[75] M. Spagnuolo, U. Andreaus, A targeted review on large deformations of planar elastic beams: extensibility, distributed loads, buckling and post-buckling, Math. Mech. Solids 24 (1) (2019) 258–280.
[76] A. Vafadar, F. Guzzomi, A. Rassau, K. Hayward, Advances in metal additive manufacturing: a review of common processes, industrial applications, and current challenges, Appl. Sci. 11 (3) (2021) 1213.
[77] J.A. Martínez-Rojas, J.L. Fernández-Sánchez, Combining dimensional analysis with model-based systems engineering, Syst. Eng. 26 (1) (2023) 71–87.